

Linköping Studies in Science and Technology  
Dissertation No. 2059

# Synthesis and Characterization of Some Nanostructured Materials for Visible Light-driven Photo Processes



**Rania Elhadi Adam**

Linköping University Studies in Science and Technology  
Dissertation No. 2059

# Synthesis and Characterization of Some Nanostructured Materials for Visible Light-driven Photo Processes

Rania Elhadi Adam



Department of Science and Technology  
Division of Physics, Electronics and Mathematics  
Linköping University, Sweden  
Norrköping 2020

Cover photo by Thor Balkhed, the photodegradation process of the Congo red dye using nanocomposite.

During the course of the research underlying this thesis, Rania Elhadi Adam was enrolled in Agora Materiae, a multidisciplinary doctoral program at Linköping University, Sweden.

Synthesis and Characterization of Some Nanostructured Materials for Visible Light-driven Photo Processes.

© Rania Elhadi Adam, 2020

Printed in Sweden by LiU Tryck, Linköping, Sweden, 2020

ISSN 0345-7524

ISBN 978-91-7929-878-4

Electronic publication: <http://www.ep.liu.se>

***Dedicated to  
My family***



# Abstract

Nanostructured materials for visible light driven photo-processes such as photodegradation of organic pollutants and photoelectrochemical (PEC) water oxidation for hydrogen production are very attractive because of the positive impact on the environment. Metal oxides-based nanostructures are widely used in these photo-processes due to their unique properties. But single nanostructured metal oxide material might suffer from low efficiency under visible light. This fact make it important to have an efficient and reliable nanocomposite for the photo-processes. The combination of different nanomaterials to form a composite configuration can produce a material with new properties. The new properties which are due to the synergetic effect, are a combination of the properties of all the counterparts of the nanocomposite.

Zinc oxides (ZnO) have unique optical and electrical properties which grant it to be used in optoelectronics, sensors, solar cells, nanogenerators, and photocatalysis activities. Although ZnO absorbs visible light from the sun due to the deep level band, it mainly absorbs ultraviolet wavelengths which constitute a small portion of the whole solar spectrum range. Also, ZnO has a problem with the high recombination rate of the photogenerated electrons. These problems might reduce its applicability to the photo-process. Therefore, our aim is to develop and investigate different nanocomposites materials based on the ZnO nanostructures for the enhancement of photocatalysis processes using the visible solar light as a green source of energy. Two photo-processes were applied to examine the developed nanocomposites through photocatalysis: (1) the photodegradation of organic dyes, (2) PEC water splitting. In the first photo-process, we used the ZnO nanoparticles (NPs), Magnesium (Mg)-doped ZnO NPs,

and plasmonic ZnO/graphene-based nanocomposite for the decomposition of some organic dyes that have been used in industries. For the second photo-process, ZnO photoelectrode composite with different silver-based semiconductors to enhance the performance of the ZnO photoelectrode was used for PEC reaction analysis to perform water splitting. The characterization and photocatalysis experiment results showed remarkable enhancement in the photocatalysis efficiency of the synthesized nanocomposites. The observed improved properties of the ZnO are due to the synergetic effect caused by the addition of the other nanomaterials. Hence, the present thesis attends to the synthesis and characterization of some nanostructured materials composite with ZnO that are promising candidates for visible light-driven photo-processes.

**Keywords:** ZnO, Nanoparticles, Nanocomposites, Heterostructures, Photocatalysis.

# Acknowledgement

This thesis has been come out due to the help, support, guidance, and collaboration from many people. Some of them are mentioned here:

I would like to express my extreme thanks and gratitude to my supervisor **Omer Nour** for his support, guidance, encouragement and help during my PhD research. Also, my sincere gratitude to my co-supervisor **Magnus Willander** for his monitoring, comments, and suggestions throughout my PhD study.

I would like to thank my co-authors **Galia Pozina**, and **Xianjie Liu** for their collaboration, useful comments and correcting of some of my manuscripts used in this thesis.

Special thanks to **Michael Hörnquist** for taking care of the FEM division at ITN and all his support.

I would like to thank all the present and past members of the **physical electronics and nanotechnology group** for their collaboration, useful discussions and the funny moments that we spent together.

My deepest appreciation to our Late research visitor **Mahsa Pirhashemi** for her collaboration, help and friendship.

I would like to thank all the team taking care of lab management and special thanks to **Anna Malmström**, **Lars Gustavsson**, **Meysam Karami Rad**, and **Thomas** for their massive work and management.



I also would like to especially thank **Ann-Christin Norén** for all the research and study administrative work.

I would like to express my thanks to **Karina Malmström** for taking care of all the administrative work of my thesis defense. Also, I would like to thank her for taking care of all Agora Materia School administrative work.

Also, I would like to thank the present and past **Agora Materia School members** for the interesting time that we spent during my PhD, and special thanks to the leaders of Agora Materia School **Per-Olof Holtz** and **Caroline Brommesson** for organizing all the fantastic events.

I appreciate the **National Energy Research Centre** (Sudan), **Ministry of Higher Education and Scientific Research** (Sudan) and **Linköping University** for the financial support.

I would like to extremely thank **my parents** for their support, unlimited love, and prayers from the faraway distance to keep me going on. I sincere appreciate my sister **Reem** and my brothers **Ammar**, **Asim** and **Ahmed** for their support, love, and encouragements.

Finally, I would like to express my deepest gratitude to my small family, my husband **Abdelgadir** for the encouragement, patient, tolerance, love and being beside me during all the hard work of my PhD. I appreciate my lovely daughter **Sireen** who made our life and stay in Sweden more tasty.

Norrköping, April 2020

Rania Elhadi Adam

# Contents

1	Introduction .....	1
1.1	Global Energy and Environmental Issues .....	1
1.2	Photocatalysis .....	2
1.3	Approaches for an Efficient Photocatalysis .....	3
2	Materials and Synthesis Methods .....	5
2.1	ZnO .....	5
2.1.1	<i>Synthesis of the ZnO NPs</i> .....	7
2.2	Mg-doped ZnO NPs .....	9
2.2.1	<i>Synthesis of Mg-doped ZnO NPs</i> .....	10
2.3	Graphene-based ZnO .....	10
2.3.1	<i>Synthesis of the ZnO/GR</i> .....	11
2.4	Silver-based ZnO Materials .....	12
2.4.1	<i>Synthesis of ZnO/GR/Ag/AgI</i> .....	13
2.4.2	<i>Synthesis of ZnO photoelectrode</i> .....	14
2.4.3	<i>Synthesis of ZnO/Ag<sub>2</sub>CrO<sub>4</sub> photoelectrode</i> .....	15
2.4.4	<i>Synthesis of ZnO/Ag/Ag<sub>2</sub>WO<sub>4</sub> photoelectrode</i> .....	16
2.4.5	<i>Synthesis of ZnO/Ag<sub>2</sub>WO<sub>4</sub>/AgBr photoelectrode</i> .....	17
3	Photocatalysis Theories .....	19
3.1	Photodegradation of Organic Dyes .....	19
3.1.1	<i>Kinetic analysis</i> .....	23
3.1.2	<i>Photodegradation Efficiency</i> .....	24
3.2	Photoelectrochemical Water Splitting .....	25
3.2.1	<i>PEC Measurements Performance</i> .....	28
3.2.2	<i>Photon to current conversion efficiency (IPCE)</i> .....	31
4	Characterization Techniques .....	33
4.1	Instruments .....	33
4.1.1	<i>X-ray diffraction spectroscopy (XRD)</i> .....	33

4.1.2	Filed emission scanning electron microscopy (FE-SEM)	34
4.1.3	Transmission electron microscopy (TEM)	36
4.1.4	X-ray photoelectron spectroscopy (XPS)	38
4.1.5	UV-Vis spectroscopy	39
4.1.6	Cathodoluminescence spectroscopy (CL)	41
4.2	Photodegradation set up	43
4.3	Three Electrodes Set-up	44
5	Results and Findings	45
5.1	Photodegradation of Organic Dyes	45
5.1.1	ZnO NPs	45
5.1.2	Mg-doped ZnO NPs	50
5.1.3	ZnO/GR/Ag/AgI nanocomposite	54
5.2	ZnO-based photoelectrode for water oxidation	58
5.2.1	ZnO/Ag <sub>2</sub> CrO <sub>4</sub> for enhanced visible-light PEC	59
5.2.2	ZnO/Ag/Ag <sub>2</sub> WO <sub>4</sub> with plasmonic behaviour for enhanced PEC	65
5.2.3	ZnO/Ag <sub>2</sub> WO <sub>4</sub> /AgBr	70
6	Conclusion and Future work	75
6.1	Conclusion	75
6.2	Future Work	78
7	References	79

## List of papers included in this thesis

1. **R. E. Adam**, G. Pozina, M. Willander, O. Nur, Synthesis of ZnO nanoparticles by co-precipitation method for solar driven photodegradation of Congo red dye at different pH, *Photonics and Nanostructures - Fundamentals and Applications*. 32 (2018) 11–18. <https://doi.org/10.1016/j.photonics.2018.08.005>.

My contribution: I prepared the samples, performed all photodegradation experiments, UV-Vis, and XRD. I was part of the SEM and CL measurements. I wrote the first draft of the manuscript.

2. **R. E. Adam**, H. Alnoor, G. Pozina, X. Liu, M. Willander, O. Nur, Synthesis of Mg-doped ZnO NPs via a chemical low-temperature method and investigation of the efficient photocatalytic activity for the degradation of dyes under solar light, *Solid State Sciences*. 99 (2020) 106053. <https://doi.org/10.1016/j.solidstatesciences.2019.106053>.

My contribution: I prepared the samples, performed all photodegradation experiments, UV-Vis, and XRD. I was part of the SEM, EDX and CL measurements. I did not perform the XPS. I wrote the first draft of the manuscript.

3. **R. E. Adam**, E. Chalangar, M. Pirhashemi, G. Pozina, X. Liu, J. Palisaitis, H. Pettersson, M. Willander, O. Nur, Graphene-based plasmonic nanocomposites for highly enhanced solar-driven photocatalytic activities, *RSC Adv.* 9 (2019) 30585–30598. <https://doi.org/10.1039/C9RA06273D>.

My contribution: I prepared the samples, performed all photodegradation experiments, UV-Vis, and XRD. I was part of the SEM

and CL measurements. I did not perform XPS and TEM. I wrote the first draft of the manuscript.

4. M. Pirhashemi, S. Elhag, **R. E. Adam**, A. Habibi-Yangjeh, X. Liu, M. Willander, O. Nur, n-n ZnO–Ag<sub>2</sub>CrO<sub>4</sub> heterojunction photoelectrodes with enhanced visible-light photoelectrochemical properties, RSC Advances. 9 (2019) 7992–8001. <https://doi.org/10.1039/C9RA00639G>.

My contribution: I was part of all the samples preparation, PEC measurements, UV-Vis, XRD, and SEM. I did not perform XPS.

5. **R. E. Adam**, M. Pirhashemi, S. Elhag, X. Liu, A. Habibi-Yangjeh, M. Willander, O. Nur, ZnO/Ag/Ag<sub>2</sub>WO<sub>4</sub> photo-electrodes with plasmonic behaviour for enhanced photoelectrochemical water oxidation, RSC Advances. 9 (2019) 8271–8279. <https://doi.org/10.1039/C8RA10141H>.

My contribution: I prepared the samples, performed all PEC measurements, UV-Vis and XRD. I was part of the SEM and EDX measurements. I did not perform the XPS. I wrote the first draft of the manuscript.

6. **R. E. Adam**, E. Mustafa, X. Liu, M. Willander, O. Nur, Visible-light driven photoelectrochemical performance of the novel ZnO/Ag<sub>2</sub>WO<sub>4</sub>/AgBr photoelectrodes.

Manuscript

My contribution: I prepared the samples, performed all PEC measurements and characterization, I wrote the first draft of the manuscript, and at present complementary experiments are ongoing work.

## List of papers not included in this thesis

1. Light-induced high-spin state in ZnO nanoparticles, Adrien Savoyant, M Rollo, Maxime Texier, **Rania E. Adam**, Sandrine Bernardini, Olivier Pilone, Olivier Margeat, Omer Nur, Magnus Willander, and Sylvain Bertaina. Nanotechnology (IOP) 31 (2020) 095707, <https://doi.org/10.1088/1361-6528/ab57f1>.

### Conference papers

2. Zinc oxide nanostructures and its nano-compounds for efficient visible light photo-catalytic processes, **Rania E. Adam**, Hatim Alnoor, Sami Elhag, Omer Nur, and Magnus Willander. Proc. SPIE 10105. Oxide-based Materials and devices VIII (2017) 101050X. doi: 10.1117/12.2254872
3. Optical and magneto-optical properties of zinc-oxide nanostructures grown by the low temperature chemical route, M. Willander, H. Alnoor, A. Savoyant, **Rania E. Adam**, and O. Nur, Proc. SPIE 10533, Oxide-based Materials and Devices IX (2018) 105331D. doi: 10.1117/12.2288970.
4. Photocatalytic properties for different metal-oxide nanomaterials, **Rania E. Adam**, Elfatih Mustafa, Sami Elhag, Omer Nur, and Magnus Willander. Proc. SPIE 10919, Oxide-based Materials and Devices X (2019) 1091925D. doi:10.1117/12.2517436.



# 1 Introduction

## 1.1 Global Energy and Environmental Issues

The fast development in our society due to the industrialization led us to a great challenge to decrease the pollution and fossil fuel usage [1]. First, the textile industry has been using a large number of organic dyes and their wastewater should be treated before exposed to the environment for reuse. The conventional method used for wastewater treatment might be expensive, not very efficient or could generate toxic secondary pollutants [2]. Therefore, an efficient, low cost and environmentally friendly methods for organic dye degradation are highly needed. Secondly, at present fossil-based fuel is the main source of energy and utilized at a high amount of consumption of which has led to global warming and climate change issues [1–4]. However, fossil fuels are depleting and its availability as a source of energy is decreasing rapidly. Accordingly, an urgent need for clean renewable sources of energy are required.

Energy from the sun is well known as a clean renewable energy source with very high potential, and it could be utilized for diverse applications. Although solar energy has been used in the household sector as well as in the industrial sector for a variety of purposes such as electrification, heating, cooling, cooking and in space technology [5], still the consumption of solar energy and others renewable energy is very little compared to fossil fuel consumption. This fact is shown in the world's total primary energy consumption diagram in Figure 1-1. Recently, solar energy has considered for photocatalysis applications including; water antibacterial disinfection, carbon dioxide reduction, pollutant degradation and photo-



catalytic water splitting to produce hydrogen ( $H_2$ )[6]. Among these photocatalysis applications, two processes were investigated in this work (1) degradation of organic pollutants and (2) PEC water splitting, which could provide an efficient solution for environmental issues and energy sustainability via a direct harnessing of the solar energy [7–9].

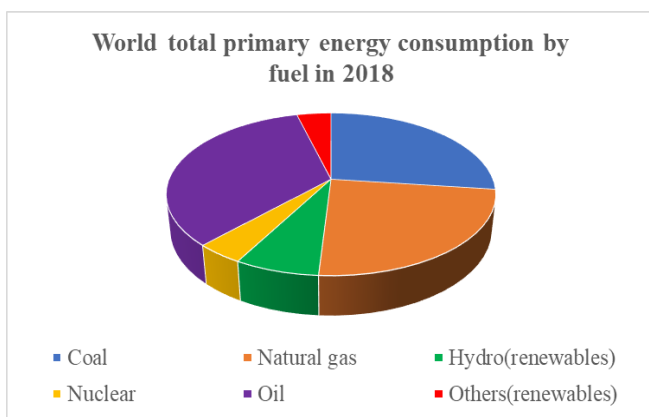


*Figure 1-1 Total world primary energy consumption by fuel in 2018 (from world energy consumption Wikipedia).*

## 1.2 Photocatalysis

Nanostructured materials based on metal oxide semiconductors that irradiated to a suitable solar light spectrum such as ultraviolet (UV) or visible light, could become a source of photogenerated electrons and holes and then to active oxygen species [10]. This unique property is the so-called photocatalysis which can be applied to a variety of environmentally friendly mechanisms.

### 1.3 Approaches for an Efficient Photocatalysis

Since the first reported photocatalysis activities for water splitting to produce  $H_2$  in 1972 using titanium dioxide ( $TiO_2$ ) semiconductor [11], a great interest in metal oxides nanostructures (NSs) have attracted researcher to develop and investigate semiconductors NSs for photocatalysis activities. NSs semiconductors have shown an improvement in photocatalysis due to their large surface area to volume ratio which provides high efficiency in photocatalysis applications.

Zinc oxide (ZnO) in its NSs forms has a potential for photocatalysis applications due to its unique properties such as; high redox potential to drive the photocatalysis reaction, high chemical and physical stability, non-toxicity, abundance, different methods for synthesis, and different NSs morphologies can be utilized [12–15].

However, the absorption in the UV range only, the photo corrosion under extremely high or low pH, and the massive recombination rate during the photocatalysis process are the main barriers for the ZnO applicability [16]. These problems could be solved by doping where additional atoms can be introduced into the ZnO such as metals and transition metals, which could reduce the recombination rate of the ZnO and then enhances the photocatalytic performance [17,18]. Also, surface modification of the ZnO by combination with another semiconductor, deposition of noble metals, or hybridization with graphene [19] to form a new nanocomposite, can suppress the recombination rate, shift the absorption into the visible light region and improve the electronic properties. Thus, enhances the photocatalytic activities.

Therefore, the goal of this thesis is to synthesis and characterization of ZnO NSs and some efficient nanocomposite materials based on ZnO and to use them as photocatalysts for photodegradation of organic dyes and

PEC water oxidation process. This goal was achieved by using different synthesis methods including the co-precipitation method, the hydrothermal chemical growth and the ultrasonic irradiation assistance. Also, different characterization techniques were used for the nanocomposite's analysis. These techniques are for optical, structural, morphological and chemical composition characterizations. In addition to that the photocatalytic experiments for photodegradation of organic dyes and PEC water splitting were performed using simulated solar light.

## 2 Materials and Synthesis Methods

### 2.1 ZnO

ZnO NSs are very attractive semiconductor for different photocatalysis processes because it possesses unique optical and electrical properties [20]. ZnO is naturally n-type, binary compound semiconductor with a wide bandgap (3.37 eV) and crystallizes in a wurtzite structure [16,20] as shown in Figure 2-1. ZnO possesses emission/absorption bands in the wavelengths range of the UV and visible light [21], which makes it suitable for photocatalysis applications. The deep level emission is originating from different native point defects (intrinsic impurities) such as oxygen vacancies ( $V_o$ ), oxygen interstitial ( $O_i$ ), zinc vacancies ( $V_{Zn}$ ), , zinc interstitial ( $Zn_i$ ), oxygen and zinc anti-site, and other native defect clusters (a combination of two different native pint defects) [22]. The native point defects could be created during the growth process of the ZnO NSs and greatly reliant on the method and the parameters of the growth [23, 24]. The presence of the native point defects provide ZnO with relatively high electron mobility ( $\sim 300 \text{ cm}^2 \text{ V}^{-2} \text{ s}^{-1}$  for the bulk ZnO and  $\sim 1000 \text{ cm}^2 \text{ V}^{-2} \text{ s}^{-1}$  for ZnO NSs [25, 26]), which enhances the electrons transfer capabilities and provide a considerable photocatalysis performance [16, 25]. Moreover, ZnO has a high redox potential that can drive various reduction and oxidation reactions during the photocatalysis process, and its wide bandgap offers an excellent driving force to induce the redox reaction [16]. In addition to that, ZnO NSs have the advantage of being grown via a variety of methods with different morphologies, besides other benefits such as non-toxicity, physical and chemical stability and abundance [12–15].

All the above-mentioned properties make ZnO NSs are appropriate candidates for photocatalysis applications.

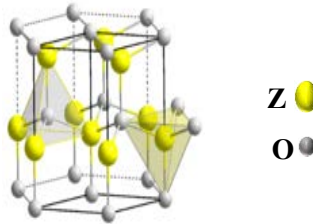


Figure 2-1 Wurtzite structure of ZnO ( [https://en.wikipedia.org/wiki/Zinc\\_oxide](https://en.wikipedia.org/wiki/Zinc_oxide)).

Although, ZnO have a variety of unique properties which give it high potential on the photocatalysis, ZnO have some drawbacks which scale down its performance in photocatalysis. ZnO absorbs mainly the UV light which compromises a small portion of the solar spectrum, and this makes it expensive when using external sources of UV light to excite the bandgap of the ZnO in order to produce electron-hole pairs. Also, the high recombination rate in the ZnO prevent the path of electron-hole outward, and then reduce the photocatalysis efficiency. The greatest drawback is that ZnO NSs get photo corrosion when immersed in solvent under the solar light due to hole trapping on the surface which is the most common issue for many NSs materials for photocatalysis [19, 27]. Another problem with the ZnO is the decomposition of the ZnO under extremely high or low pH values [19]. Many studies showed that ZnO can dissolve in high acidic media or in strong basic media under the illumination of light or under-voltage biases [25, 26].

Many research works concerning overcoming these issues with ZnO to improve its photocatalysis performance through composite with other materials focusing on different approaches such as doping etc.. have been published [29–33]. Deposition of metals [34], composite ZnO with other semiconductors, and hybridization of the ZnO with graphene are some examples [35–39]. Therefore, we are investigating different strategies for coupling ZnO NSs with other nanomaterials and produce a novel new nanocomposite for the enhancement of the ZnO photocatalyst performance to degrade organic dyes and for water splitting through water oxidation.

### **2.1.1 Synthesis of the ZnO NPs**

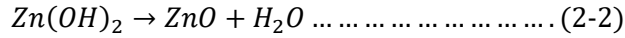
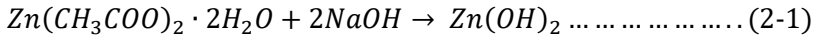
Many methods can be applied for synthesis of ZnO NPs for the degradation of organic dyes which include the hydrothermal, sol-gel, solvothermal, and co-precipitation methods [38, 39]. Using the different methods and different growth parameters will lead to the synthesis of different ZnO NPs sizes and shapes. Among these methods, the co-precipitation is favourable because it is simple, it only requires a source of zinc and a precipitating agent. Then different parameters such as the precursor concentration, time of growth and temperature could be applied to have ZnO NPs with various shapes and sizes. Different synthesis methods for ZnO NPs with different precursors and temperatures are presented in *Table 2-1*.

*Table 2-1 Summary of different methods, precursors and temp. of ZnO NPs synthesis.*

Synthesis method	Precursors	Reaction temperature	Reaction time	Further heating	References
precipitation	Zinc acetate dihydrate Ammonia	85 °C	3-65 min.	Drying 60°C 10 h	[40]
precipitation	Zinc nitrate hexahydrate Sodium hydroxide	25 °C	2h	Drying 100 °C 2 h	[41]
Solvothermal	Zinc acetate dihydrate Triethanolamine Methanol	150 °C	18 h	Drying 60 °C overnight	[42]
Hydrothermal	Zinc acetate dihydrate Methanol	150 °C	6 h	Air drying 2 h	[43]
Hydrothermal	Zinc chloride Sodium hydroxide	100-220 °C	5-10 h	Drying at room temp.	[44]
Thermolysis	Zinc acetate dihydrate	550 °C	10 h	-	[45]
Microwave assisted	Zinc acetate dihydrate Ethylene glycol	-	1 h	Microwave irradiation 200-600 W	[46]

In this thesis ZnO NPs were synthesized by co-precipitation method as follows: we used 4.39 g (0.1 M) of the zinc acetate dihydrate ( $\text{Zn}(\text{CH}_3\text{COO})_2 \cdot 2\text{H}_2\text{O}$ ) with 100 ml deionized (DI) water for the zinc precursor. Another solution was prepared using a 1.599 g (0.2 M) of sodium hydroxide (NaOH) dissolved in DI water. The two solutions were magnetically stirred for 10 minutes, then they were poured into one beaker and kept under magnetic stirring for 2 hours at 750 rpm and temperature of 60 °C on a hot plate [20, 42]. By using centrifugation for 2 minutes at 4500 rpm, the precipitating product was separated from the solution [20, 42]. The precipitate was washed with DI for several times then one time

with acetone to remove undesired particles. Finally, ZnO NPs was obtained after drying the precipitating product at 75 °C for 6 hours in a pre-heated oven [20,42,43]. It is worth to note that the alkaline ratio to Zn<sup>2+</sup> is important for the ZnO NPs formation, thus the number of moles of OH<sup>-</sup> to Zn<sup>2+</sup> should be 1: 2 or higher [44]. This is because the growth of the ZnO starts by the precipitation of zinc hydroxide (Zn(OH)<sub>2</sub>), then converted to the ZnO NPs according to the following chemical reaction [49, 50]:



## 2.2 Mg-doped ZnO NPs

In order to utilize the photocatalysis more efficiently, it is necessary to synthesis an efficient photocatalysts under solar light [47]. Some elements such as (Mg, Cd, Co, and Mn) can be used as a dopant to improve the photocatalysis activities of the ZnO under the illumination of solar light [51, 52]. Among these elements, magnesium (Mg) is attractive for doping ZnO because of the similar ionic radius (0.57 and 0.60 Å for Mg and Zn respectively), thus the high probability of incorporation of Mg<sup>2+</sup> into the ZnO crystal lattice is expected. This incorporation will tune the bandgap of the ZnO and then increase the absorption of light which improves the photocatalytic efficiency of organic dyes[17, 53–55]. Also, the incorporation of Mg<sup>2+</sup> into the ZnO will cause superior textural properties and efficient separation of electron-hole which enhances the solar-driven photocatalytic efficiency [47].



### 2.2.1 Synthesis of Mg-doped ZnO NPs

For the synthesis of Mg-doped ZnO NPs, a diluted solution of magnesium nitrate hexahydrate  $\text{Mg}(\text{NO}_3)_2 \cdot 6\text{H}_2\text{O}$  with different atomic concentrations relative to Zn (0, 3, 5, and 7%) were prepared then mixed with 0.2 M of NaOH solution and stirred overnight at room temperature [42]. Then, 0.1 M of the  $(\text{Zn}(\text{CH}_3\text{COO})_2 \cdot 2\text{H}_2\text{O})$  solution was added to the above mixture and stirred at 750 rpm for 2 hours under a temperature of 60 °C in a hot plate. Then, the precipitating product was separated by using centrifugation at 4500 rpm for 2 minutes then it was washed several times with DI water and one time with acetone. Mg-doped ZnO NPs with different doping concentrations (0, 3, 5, and 7%) were obtained by drying of the precipitate product into a preheated oven at 75 °C for 6 hours [25, 47].

## 2.3 Graphene-based ZnO

Graphene (GR) is a two-dimensional (2D) material and its carbon atoms are assembled in a honeycomb lattice structure formed by  $\text{sp}^2$  hybridized atomic orbital consisting of sigma bonds between carbon atoms and pi bond out of the plane [36,51,52] as shown in Figure 2-2. GR possesses many interesting electronic properties, such as high charge carrier mobility up to  $10^6 \text{ cm}^2\text{V}^{-1}\text{s}^{-1}$  with low resistivity ( $0.1\text{--}6 \text{ K}\Omega/\square$ ), relatively very large surface area to volume ratio, and high optical transparency over a very large spectral range from IR to UV [33–37, 57], which makes it an excellent candidate for enhancing the performance of photocatalysts due to the improved separation efficiency of photogenerated electron-hole pairs during the photocatalytic processes [33, 34, 57–61]. Particularly, ZnO/GR nanocomposite is interesting due to the capability of inhibiting

the recombination of photogenerated charge carriers during the photocatalytic process. It is worth to note that the amazing properties of the honeycomb carbon structures are not really new, it is abundant and naturally occurring in the form of graphite which has been used as minerals for a long time [58]

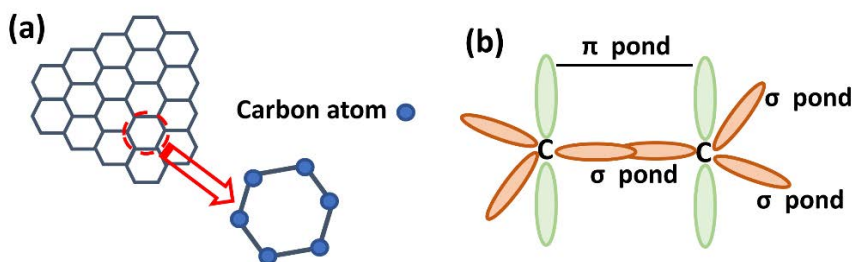


Figure 2-2 (a) Graphene lattice structure, (b)  $SP^2$  hybridized orbitals of carbon atoms.

### 2.3.1 Synthesis of the ZnO/GR

The ZnO/GR nanocomposite was synthesized according to our published work [52], by the dispersion of GR powder ( $10 \text{ mg.l}^{-1}$ ) into  $\text{Zn}(\text{CH}_3\text{COO})_2 \cdot 2\text{H}_2\text{O}$  solution ( $0.01 \text{ M}$ ). Then potassium hydroxide (KOH) solution ( $0.05 \text{ M}$ ) was added drop wise under ultrasonic water bath for 10 minutes at  $60^\circ\text{C}$ . Then, by centrifugation at 3000 rpm for 10 minutes the precipitating product was separated. Afterword, the precipitate was washed with DI water and acetone three times. The ZnO/GR nanocomposite was obtained after drying the precipitate overnight in a preheated oven at  $120^\circ\text{C}$ . The preparation process of the ZnO/GR nanocomposite is presented in Figure 2-3.

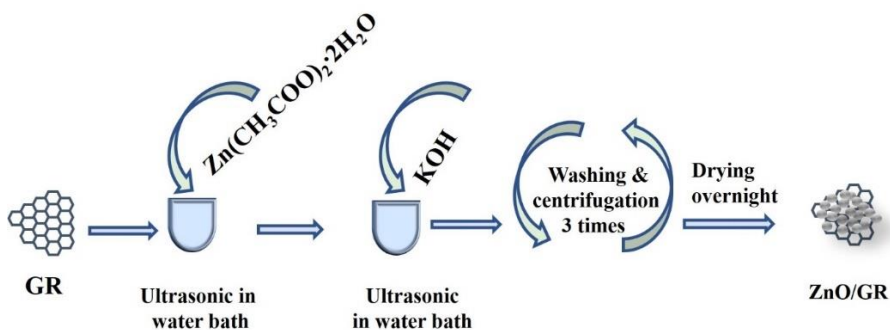
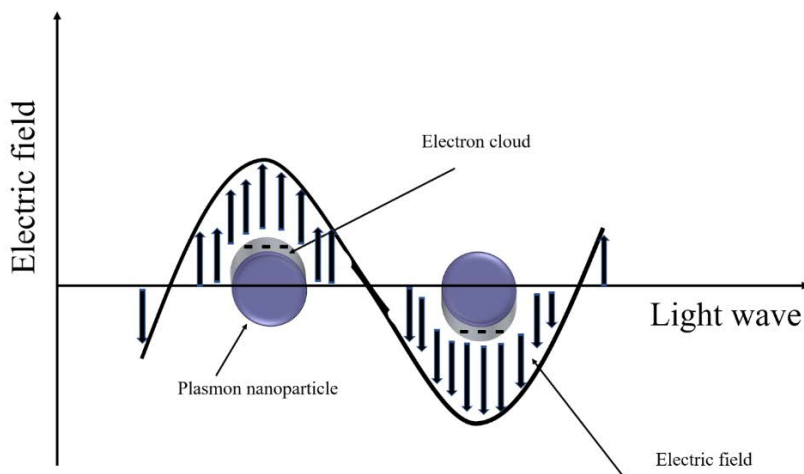


Figure 2-3 The preparation process of ZnO/GR nanocomposite.

## 2.4 Silver-based ZnO Materials

Ag compounds materials have been considered as a promising candidate to be used as co-catalysts to enhance photocatalytic efficiency [59]. The deposition of Ag-materials on the surface of ZnO can improve the photocatalytic performance due to the surface plasmon resonance (SPR) effect of metallic silver [60]. The SPR is a collective oscillation of electrons induced by the electromagnetic field of the incident visible light which enhances the photocatalytic process [60,61] (see Figure 2-4) and it depends on the size and shape of the plasmon particles [62]. The existence of the SPR can enhance the absorption of the catalyst by confining or scattering the light into the photocatalyst [61]. Also, the SPR allows absorption of visible light in higher wavelength which then extend the absorption range of the light [61]. Consequently, electronic and photocatalytic properties of the photocatalyst will be improved. Therefore, different Ag-based semiconductors were prepared and their characteristics for photocatalysis performance were investigated in this thesis, which includes AgI,  $\text{Ag}_2\text{CrO}_4$ ,  $\text{Ag}_2\text{WO}_4$  and AgBr. These Ag- compound semiconductors were

nanocomposite with ZnO to produce new heterostructure with effectively enhanced photocatalysis performance.



*Figure 2-4 Illustration of the surface plasmon resonance in a plasmon nanoparticles.*

#### **2.4.1 Synthesis of ZnO/GR/Ag/AgI**

ZnO/GR/Ag/AgI nanocomposites were synthesized according to our previous published work [52] using different AgI percentage by dispersion of the as-prepared ZnO/GR in a 200 ml of DI water under ultrasonic irradiation for 10 minutes. Then a  $\text{AgNO}_3$  powder was added to the mixer and kept under stirring for 30 minutes. Afterword, NaI was dissolved in DI water with three different weight ratios (10%, 20%, and 30%) and added dropwise to the above mixture and kept under ultrasonic irradiation for one hour. By using the centrifugation, the product was separated and washed two times with DI water and one time with acetone to remove any undesired salt. Finally, by drying the product in a preheated oven at 75 °C for 6 hours, the ZnO/GR/Ag/AgI

nanocomposites were obtained successfully. The synthesis process of the ZnO/GR/Ag/AgI nanocomposites are explained in Figure 2-5 [52]. It is worth to note that the Ag particles could be introduced in the nanocomposite during the sample preparation, or during the irradiation of the visible solar light due to the photoreduction reaction.

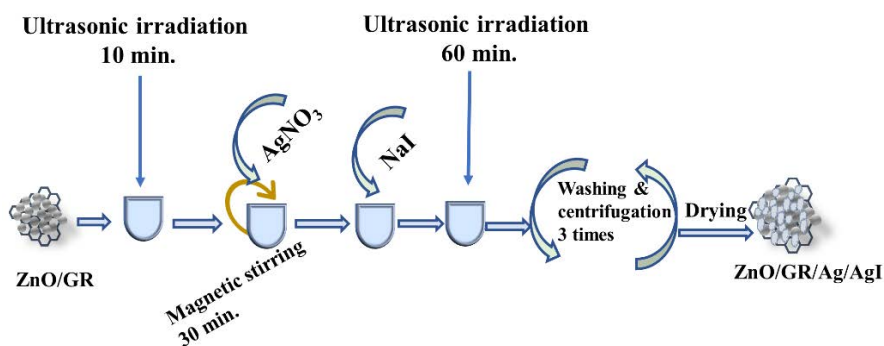


Figure 2-5 The preparation process of ZnO/GR/Ag/AgI nanocomposite.

### 2.4.2 Synthesis of ZnO photoelectrode

A clean conductive substrate such as Au coated glass or fluorine tin oxide (FTO) were used to grow ZnO nanorods (NRs) as described in our previous publications [63, 67] through the following steps:

1. The substrates were cleaned with acetone, isopropanol, and DI water, subsequently using ultrasonic bath for 10 min.
2. Seed solution preparation: 0.03 M potassium hydroxide (KOH) was dissolved in 125 ml methanol and added dropwise into a 0.01 M of  $\text{Zn}(\text{CH}_3\text{COO})_2 \cdot 2\text{H}_2\text{O}$  dissolved in a 65 ml methanol. The mixture was magnetically stirred at 750 rpm for 2 h in a hot plate at 60 °C. Then the temperature was turned off and the seed solution was kept under magnetic stirring overnight.

3. Using spin coating at 3000 rpm for 25 s, the seed solution deposited on to the substrate and this process was repeated three times to obtain good coverage of the ZnO NPs onto the substrate to allow condense growth of the ZnO NRs. Then, the substrates were annealed into an air in an oven at 120°C for 10 min. to let the seeds attached to the substrates.
4. The precursor solution of the growth was prepared using equal molecular concentrations (0.05 M) of zinc nitrate hexahydrate ( $\text{Zn}(\text{NO}_3)_2 \cdot 6\text{H}_2\text{O}$ ) and hexamethylenetetramine (HMT) in 100 ml DI water. The seeded substrates prepared in step 3 were fixed into Teflon samples holder and immersed horizontally facing down in the precursor solution. Then the samples were loaded into a preheated oven at 90 °C for 5 hours. After cooling down to room temperature, the samples were washed with DI water and dried with blowing nitrogen.

### **2.4.3 Synthesis of ZnO/Ag<sub>2</sub>CrO<sub>4</sub> photoelectrode**

Silver chromate Ag<sub>2</sub>CrO<sub>4</sub> nanoparticles were deposited over the above prepared ZnO NRs photoelectrode using successive ionic layer adsorption and reaction (SILAR) method followed by annealing process [63]. SILAR method implies immersion of the substrate into cationic precursor, then rinse with DI water, flowed again by immersion into the anionic precursor and then rinse again with DI water to complete one SILAR cycle as shown in Figure 2-6. A SILAR cycle can be repeated several times to have enough particles on the ZnO. Herein Ag<sub>2</sub>CrO<sub>4</sub> particles deposit on the ZnO NRs using the SILAR method at room temperature as follows and as described in our previous work [63]: first ZnO NRs immersed into 0.05 M AgNO<sub>3</sub> solution (20 ml) for 2 min. Then the substrates were

washed with methanol to remove the excess of reagent and dried by blowing nitrogen. Secondly, the substrate was immersed into 0.05 M of sodium chromate ( $\text{Na}_2\text{CrO}_4$ ) solution (20 ml) for 2 min., again the sample was washed and was dried by blowing nitrogen. SILAR cycle was repeated for several times producing dark purple samples. Finally, the prepared  $\text{ZnO}/\text{Ag}_2\text{CrO}_4$  photoelectrodes were dried for 1 h at 60 °C.

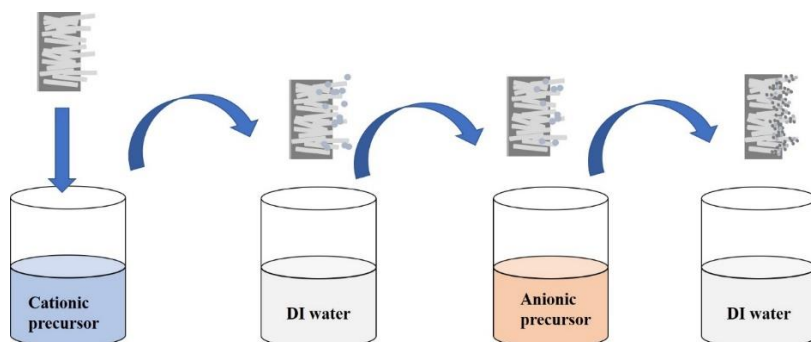


*Figure 2-6 SILAR method to deposit particles into ZnO NRs.*

#### **2.4.4 Synthesis of $\text{ZnO}/\text{Ag}/\text{Ag}_2\text{WO}_4$ photoelectrode**

$\text{Ag}/\text{Ag}_2\text{WO}_4$  nanoparticles were deposited into the ZnO NRs using the SILAR method. A 0.05 M solution of  $\text{Ag}(\text{NO}_3)_3$  and 0.05 M of sodium tungstate ( $\text{Na}_2\text{WO}_4 \cdot 2\text{H}_2\text{O}$ ) were used as cationic and anionic aqueous precursors, respectively as shown in Figure 2-6. ZnO NRs photoelectrode was immersed into the  $\text{AgNO}_3$  solution (20 ml DI water) solution for 2 minutes to absorb silver ions ( $\text{Ag}^+$ ). Then the photoelectrodes were washed with DI water to remove the excess ions. After that, the photoelectrodes were immersed in the  $\text{Na}_2\text{WO}_4 \cdot 2\text{H}_2\text{O}$  solution for 2 min. and

washed with DI water to complete one SILAR cycle. This cycle was repeated several times to obtain enough Ag/Ag<sub>2</sub>WO<sub>4</sub> particles on the ZnO NRs.

#### **2.4.5 Synthesis of ZnO/Ag<sub>2</sub>WO<sub>4</sub>/AgBr photoelectrode**

AgBr was deposit into ZnO/ Ag/Ag<sub>2</sub>WO<sub>4</sub> photoelectrode by ion exchange of Ag<sub>2</sub>WO<sub>4</sub> into AgBr using the hydrothermal treatment. First, 0.1 M (0.3 g) of sodium bromide (NaBr) dissolved into 30 ml DI water, then the as-prepared ZnO/Ag/Ag<sub>2</sub>WO<sub>4</sub> was immersed horizontally facing up into the NaBr solution and it was loaded to a preheated oven at 90 °C for 5 hours. After the photoelectrode was cooled down to room temperature, it was ultrasonically washed with DI water, and dried with blowing nitrogen.





### 3 Photocatalysis Theories

#### 3.1 Photodegradation of Organic Dyes

A catalyst with suitable band edge position is important to perform the photocatalytic reaction. The band edge energy of the ZnO with other interesting semiconductors are presented in Figure 3-1, which shows their potentials for photocatalysis activities [6]. According to the positions of the conduction /valence (CB/VB) band and the redox potentials of the reactions, the semiconductors can be strongly oxidative, strongly reductive, or having reasonable oxidation and reduction reaction [6]. The strongly oxidative catalysts have high VB levels for water oxidation reactions (e.g. ZnO). Whereas, the strongly reductive catalysts have a high CB level suitable for CO<sub>2</sub> reduction reaction and H<sub>2</sub> evaluation reaction [64]. However, the CB and VB edge potentials of a semiconductor at zero point charge can be calculated using the electronegativity theory [63, 69, 70]:

$$E_{VB} = \chi - E_e + 0.5 E_g \dots \dots \dots (3-1)$$

$$E_{CB} = E_{VB} - E_g \dots \dots \dots (3-2)$$

where E<sub>VB</sub> and E<sub>CB</sub> are the VB and CB edge potentials,  $\chi$  is the absolute electronegativity of the semiconductor, E<sub>e</sub> is the energy of free electrons on the hydrogen scale (~4.5 eV), and E<sub>g</sub> is the bandgap energy of the semiconductor.

Therefore, it is possible to calculate the  $E_{VB}$  and  $E_{CB}$  for the nanocomposite materials and propose the photocatalysis mechanism accordingly (more information are provided in paper IV and V [59,67].

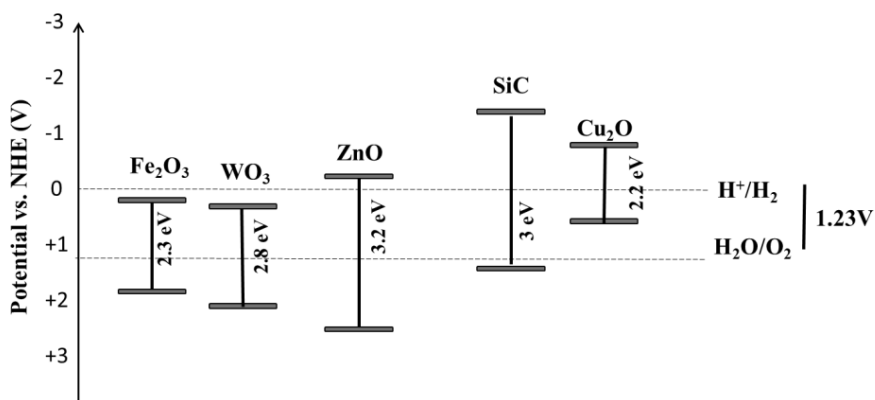


Figure 3-1 Band edge energy consideration for some interesting catalysts [6].

However, in the photocatalysis process for dye degradation the photons with suitable energy for the catalyst bandgap can create electron-hole pairs [9, 19-22]. Electrons in the CB will be captured by oxygen molecules ( $O_2$ ) to produce hydroxyl radical ( $OH\cdot$ ), superoxide radical ( $O_2^{\cdot-}$ ), and hydroperoxyl radical ( $HO_2$ ) [68]. On the other hand, holes in the VB will react with water molecules ( $H_2O$ ) and hydroxyl ions ( $OH^-$ ) to form  $OH\cdot$  [68]. The overall mechanism of dye degradation by the semiconductor under solar light is presented in Figure 3-2. All radical species that produced will attack the organic dye leading to the decomposition or mineralization of the dye into a final product according to the following reaction [20].

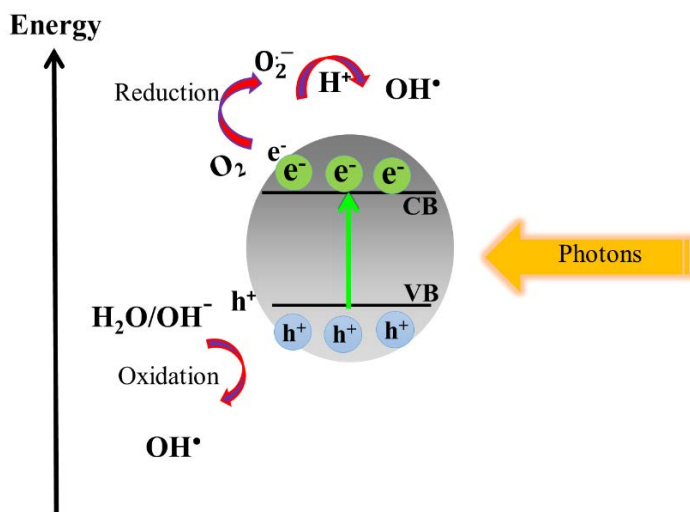
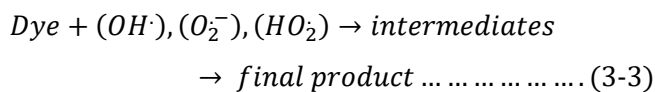
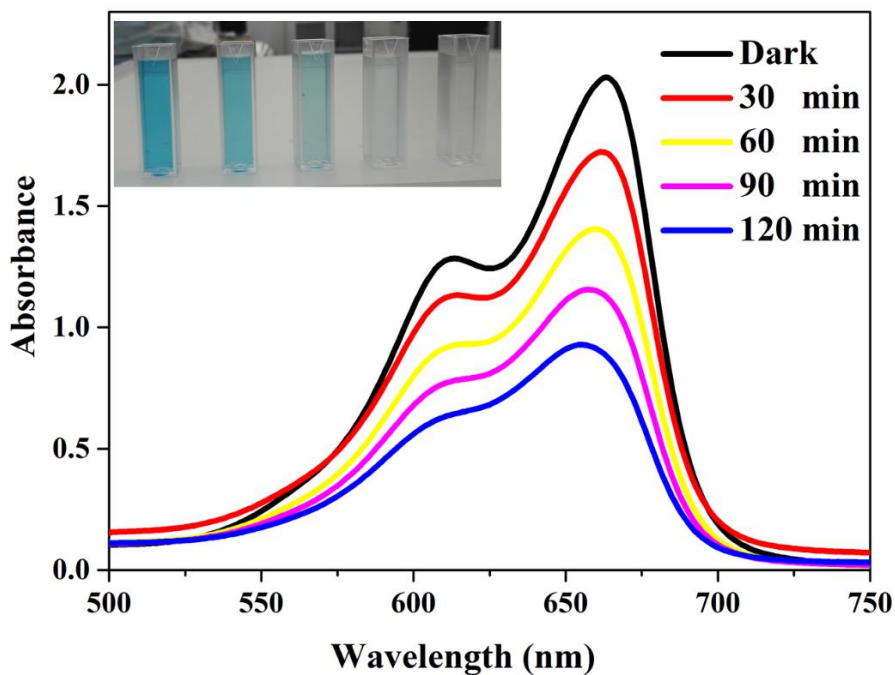


Figure 3-2 Photocatalytic mechanism for dye photodegradation.

The organic dye could be degraded through direct mineralization or stepwise N-deethylation process. The direct mineralization produces gaseous as end products such as  $\text{CO}_2$ ,  $\text{NO}_3$ , and  $\text{NO}_x$  [52]. Whereas in the stepwise N-deethylation process the conjugated structure of the dye will be destroyed. If the measured absorption spectrum of the dye during the photocatalysis reaction time detected without any shift, the dye is directly mineralized, otherwise, it is a stepwise N-deethylation process [39, 69, 70]. Figure 3-3 shows the UV-Vis absorbance spectrum of methylene blue (MB) dye during the photocatalysis reaction with Mg-doped ZnO NPs. The inset shows the discoloration of the MB dye. However, many factors can affect the photocatalytic reaction and the degradation rate of the dyes.

These factors include the source of light and its intensity, catalyst amount, type of the dye, reaction time and pH of the dye solution.



*Figure 3-3 Absorbance spectra of MB dye during the photocatalysis reaction. The inset shows the colour of MB changing to transparent.*

The organic dyes could be classified as an anionic or cationic dye. Congo red (CR) and MB are used in this thesis as a model dye. CR is an anionic dye which is more acidic, and when dissolved in water it will become negatively charged, which allow its adsorption by the positive surface of the catalyst [75]. Whereas MB is a cationic/basic dye and its surface is positively charged, therefore electrons in the CB will be migrated to the surface of the catalyst and attack the molecular structure of the dye leading

to the decomposition of the dye [76]. The chemical structures of the CR and the MB are presented in Figure 3-4.

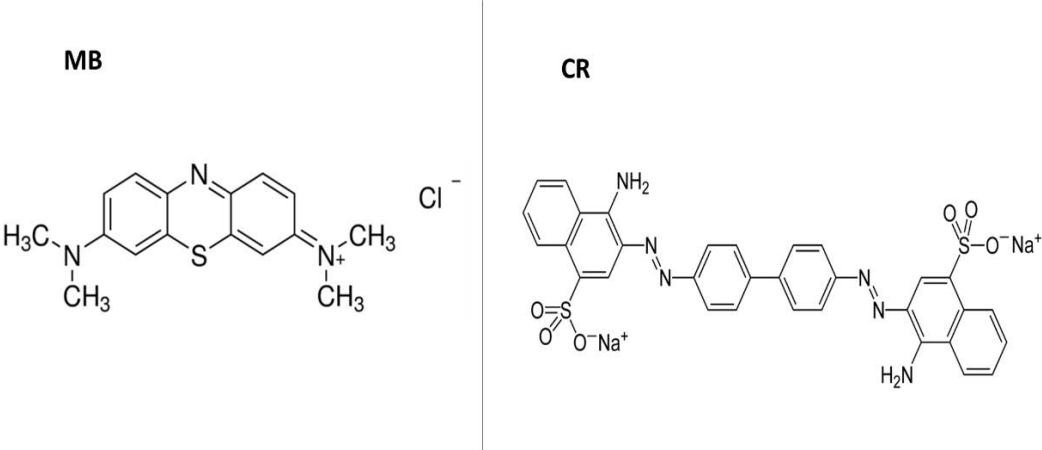


Figure 3-4 Chemical structure of MB (left) and CR (right) dye

### 3.1.1 Kinetic analysis

A photocatalytic mechanism should follow the Langmuir-Hinshelwood’s pseudo-first-order kinetic model [73], where the apparent reaction constant for the photocatalyst is determined according to equation (3-4).

$$K_{app} = \frac{\ln \left[ \frac{C_0}{C} \right]}{t} \dots \dots \dots (3-4)$$

where  $K_{app}$  is the apparent reaction constant (min<sup>-1</sup>),  $C_0$  is the initial concentration of the dye (mol l<sup>-1</sup>),  $C$  is the dye concentration after irradiation time  $t$  (mol l<sup>-1</sup>) and  $t$  is the irradiation time (min.), The plot of  $\ln \left[ \frac{C_0}{C} \right]$  versus irradiation time for the ZnO NPs with different nanocomposites are shown in Figure 3-5.

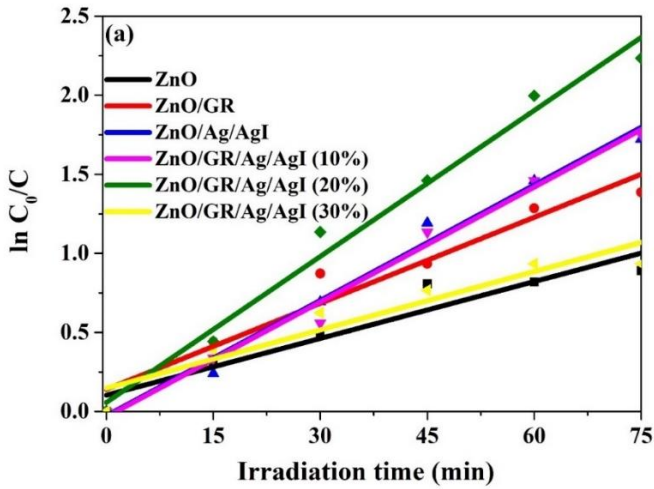


Figure 3-5 The plot of  $(\ln C_0/C)$  vs. illumination time for ZnO NPs and different synthesized nanocomposites based on ZnO NPs.

### 3.1.2 Photodegradation Efficiency

The photodegradation efficiency (%) versus irradiation time can be estimated from the UV-vis absorbance spectra measurement according to equation (3-5).

$$\text{Photodegradation (\%)} = \frac{A_0 - A}{A_0} \times 100 \dots \dots \dots (3-5)$$

Where  $A_0$  is the initial maximum absorbance of the dye, and  $A$  is the absorbance after a specific irradiation time.

## 3.2 Photoelectrochemical Water Splitting

The PEC water splitting needs (1) a semiconductor in a form of Schottky junction to absorb light and generated charge carriers (electron-hole pairs), (2) separation of the photogenerated charge carriers, and (3) charge carriers collection and transportation. As shown in Figure 3-6 below. The suitable semiconductor for water splitting should meet the following criteria:

1. Suitable bandgap which is small enough to absorb a large range of sunlight, and large enough to split water (larger than electron energy  $>1.23$  eV)
2. Suitable band edge; the position of the CB of the semiconductor should be higher than the  $H_2/H_2O$  level, whereas the VB position should be lower than  $H_2O/O_2$  level.
3. Long charge carrier lifetime and higher charge carrier mobility which results in fast charge carrier transportation (Table 3-1) shows some typical metal oxides photoelectrodes with their charge carrier mobility and lifetime [23, 78, 79].



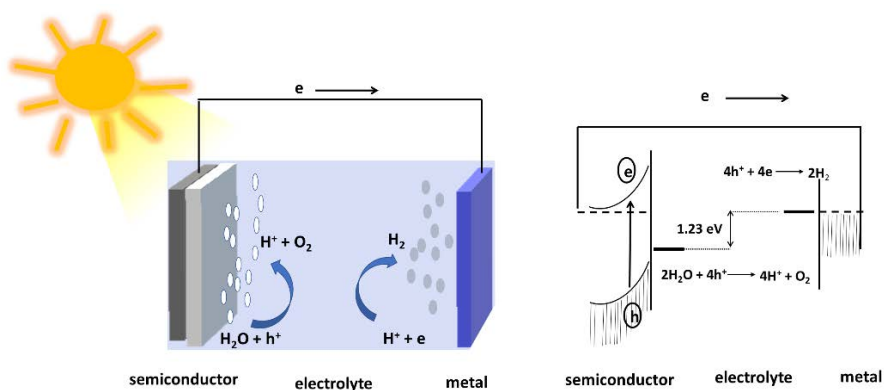
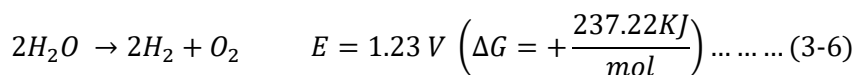


Figure 3-6 Basic principle of PEC water splitting with Schottky junction.

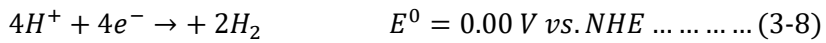
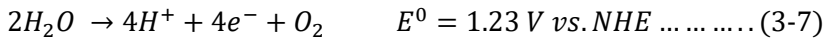
Material	Charge carrier mobility ( $\text{cm}^2 \text{V}^{-1} \text{s}^{-1}$ )	Charge carrier lifetime (s)
$\text{Fe}_2\text{O}_3$	0.5	$0.003 \times 10^{-9}$
$\text{WO}_3$	10	$1-9 \times 10^{-9}$
$\text{Cu}_2\text{O}$	6	$0.40 \times 10^{-9}$
$\text{BiVO}_4$	0.044	$40 \times 10^{-9}$
$\text{ZnO}$	300	$0.1-1 \times 10^{-9}$

Table 3-1 The charge carrier mobility and lifetime of some metal oxides photoelectrodes

The overall water splitting reaction can be summarized as follows:



Equation (3.6) theoretically explains that the minimum requirement for water splitting into hydrogen and oxygen molecules is 1.23 V at the standard temperature ( $T^0=298K$ ) and pressure of ( $P^0=1$  bar) [74]. The chemical reaction in equation (3-6) can be written into two relevant equations at (pH =0):



But practically, overpotential is required due to different electrode materials, the electrolyte used and the distance between the electrodes. This reaction is performed at two different electrodes locations which are the photoanode/semiconductor where oxidation reaction arises and oxygen is produced, and the cathode where reduction reaction arises and hydrogen is produced (see Figure 3-6). If the photoanode is an n-type semiconductor, the photogenerated holes moves to the surface of the semiconductor to drive the water oxidation reaction, while electrons migrate to the bulk of the photoelectrode to reach the back contact, then to the metal electrode through a wire to perform water reduction. If the photoanode is a p-type semiconductor, the photogenerated electrons migrate to the surface of the semiconductor to drive the water reduction, while holes should migrate to the bulk of the semiconductor to reach the back contact, then to the metal electrode through a wire to perform water oxidation.

### 3.2.1 PEC Measurements Performance

In order to study the PEC performance and water splitting analysis, the charge carrier characteristics at the semiconductor/electrolyte interface for the synthesized nanocomposites should be performed with three - electrodes configuration. This can be obtained from the photocurrent density versus the applied potential through the linear sweep voltammetry (LSV) measurements as shown in Figure 3-7(a) for the ZnO NRs. Which shows the LSV curves in the dark and under illumination of solar light. It could be observed that negligible photocurrent is detected in the dark, while the photocurrent increased obviously under illumination of solar light. The photo response over time also could be investigated through chronoamperometry measurements and the photocurrent density versus time can be recorded and analysed as shown in Figure 3-7(b). More details on the PEC performance and results of the synthesized nanocomposites are discussed in chapter 5.

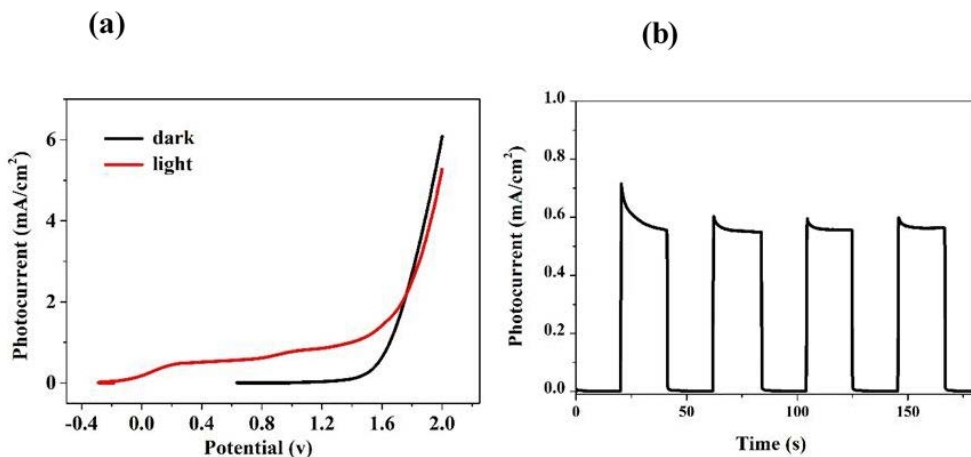
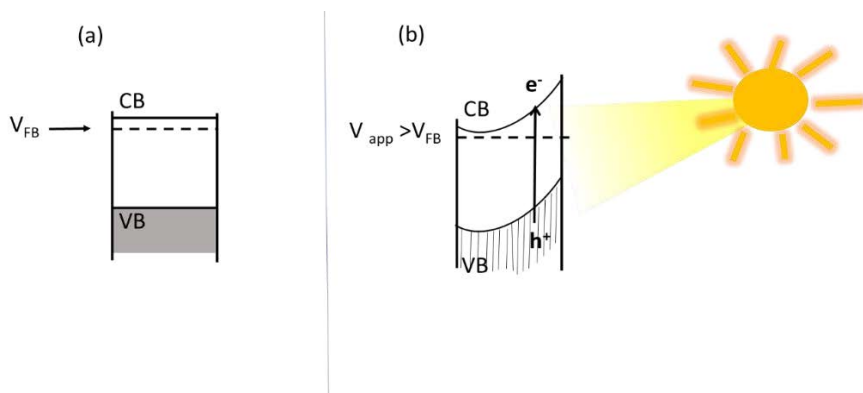


Figure 3-7 (a) LSV curves in dark and light conditions, and (b) photo response over time for ZnO NRs photoelectrode.

From the electrochemical impedance measurement under dark, we can get the Mott-Schottky plot where the flat band potential ( $V_{FB}$ ) could be extracted. At the  $V_{FB}$  no band bending occurs at the semiconductor-electrolyte junction, so the CB and VB are flat as shown in Figure 3-8(a) for the n-type semiconductor-based photoelectrode. If the photoelectrode is illuminated with light or biased with an applied potential ( $V_{app}$ ) greater than the  $V_{FB}$ , the conditions of  $V_{FB}$  are not valid. In this case, the relative change in the charge carriers concentration leads to the photocatalysis reaction [74] (Figure 3-8(b)).



*Figure 3-8 The band position of n-type semiconductor (a) at the flat band condition, and (b) under illumination of solar light.*

During the  $V_{FB}$  measurements, the capacitance of space charge layer ( $C_{sc}$ ) is recorded and  $(1/C_{sc})$  versus the applied potential is plotted as shown in Figure 3-9 [67] for the synthesized ZnO NRs and ZnO/Ag/Ag<sub>2</sub>WO<sub>4</sub> photoelectrodes grown on FTO by the hydrothermal method [59]. The intercept of the linear regression is the  $V_{FB}$  which is +0.60 and +0.4V for the ZnO and ZnO/Ag/Ag<sub>2</sub>WO<sub>4</sub> photoelectrodes, respectively. The plot is following the Mott-Schottky equation given in equation (3-9).

$$1/C_{sc}^2 = \frac{2}{\epsilon\epsilon_0 eNdA^2} \left( V_{app} - V_{FB} - \frac{kT}{e} \right) \dots \dots \dots (3-9)$$

where  $\epsilon$  is the permittivity of the semiconductor and  $\epsilon_0$  and is the permittivity of the vacuum,  $N_d$  is the charge carrier density, and  $A$  is the area of the photoelectrode.

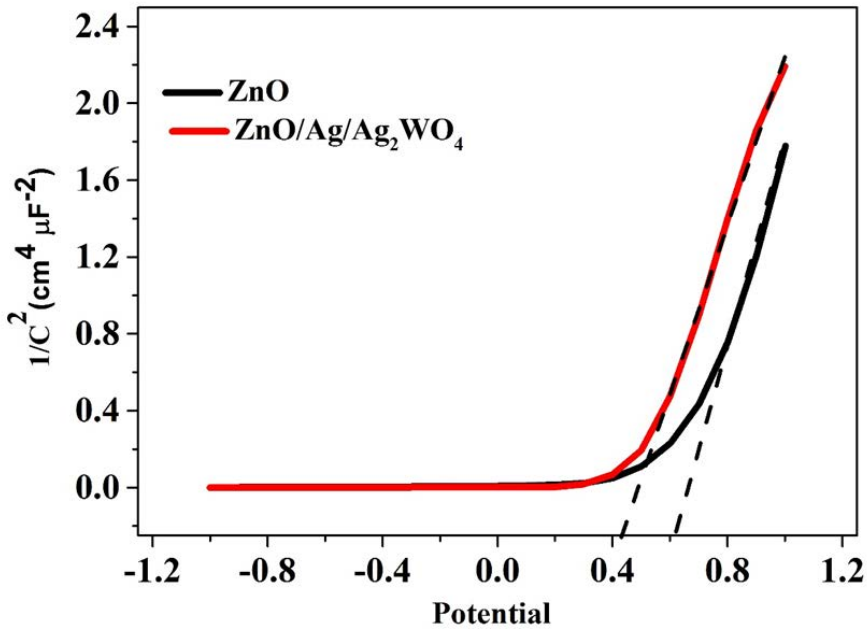


Figure 3-9 Mott-Schottky plots of  $1/C^2$  versus applied potential (V) in complete darkness at a frequency of 3 kHz for the ZnO NRs, and the ZnO/Ag/Ag<sub>2</sub>WO<sub>4</sub> photo-electrodes.

### 3.2.2 Photon to current conversion efficiency (IPCE)

The IPCE can be studied for more PEC analysis. It is a measure of how efficient a photoelectrode in converting an individual photon to an extractable electron [74]. The measurement performed with a monochromator light source for spectral distribution that can be selected by the wavelength, and at the same time, the current density generated at each wavelength should be measured. Then IPCE can be calculated from equation (3-10) [76]:

$$IPCE(\%) = \frac{1240 \times I_{ph}}{\lambda \times J} \times 100 \dots \dots \dots (3-10)$$

Where  $I_{ph}$  is the photocurrent density,  $\lambda$  is the wavelength of the incident light and  $J$  is the intensity of the incident light.



## 4 Characterization Techniques

### 4.1 Instruments

#### 4.1.1 X-ray diffraction spectroscopy (XRD)

Philips powder XRD diffractometer using Cu Ka radiation and wavelength of 0.15406 nm was used to investigate the structural properties of the nanomaterials. The generator was adjusted at a voltage of 40 kV and a current of 40 mA to carry out the measurements. From the XRD measurements, we can obtain information about the crystallinity of the samples where the crystalline structure of the sample makes the incident of the monochromatic x-ray beam with incident angle ( $\theta$ ) and wavelength ( $\lambda$ ) to be diffracted into specific directions as shown in Figure 4-1. Where the diffracted beam collected at the detector at ( $2\theta$ ) according to Bragg's law [77]:

$$n\lambda = 2d\sin(\theta) \dots \dots \dots (4-1)$$

Where  $n$  is the diffraction order,  $d$  is the distance between the diffraction plane,  $\lambda$  is the x-ray wavelength, and  $\theta$  is the Bragg diffraction angle. Accordingly, the density of electrons and distance between neighbour atoms could be determined. From the angles and the higher intensities of the diffracted beams due to effective interference, a pattern of XRD intensities vs. ( $2\theta$ ) could be obtained. The study of this pattern will give information about crystal structure and orientation. Also, we can calculate the crystallite size of the NPs using Scherrer equation [78]:

$$D = \frac{k\lambda}{\beta_{hkl}\cos\theta} \dots \dots \dots (4-2)$$



where  $D$  is the crystallite size of the NPs,  $\lambda$  is the x-ray wavelength,  $\theta$  is the Bragg diffraction angle,  $\beta$  is the full width at the half maximum (FWHM) of the highest peak, and  $k$  is Scherrer constant = 0.9.

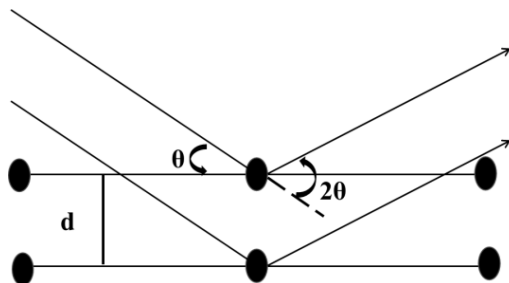


*Figure 4-1 Principle of XRD*

#### **4.1.2 Field emission scanning electron microscopy (FE-SEM)**

FE-SEM (Quanta 200 FEG) was used to study the morphology of the synthesized ZnO and its nanocomposites with an accelerating voltage of 30.0 kV. From the FE-SEM imaging we can obtain information about the shape, the size distribution, and dimensions of the nanocomposites. The FE-SEM is composed of electron source, electromagnetic lenses, and electron detector. An electron beam with high energy is accelerated and focused by the lenses on the surface of the sample. Then the sample emits secondary electrons which can be detected. The emitted secondary electrons number are varied due to the surface variation of the sample. The SEM image is created by scanning the beam over the surface of the sample in a raster way and detecting the variation of electrons number that

emitted from the surface of the sample as shown in the schematic diagram in Figure 4-2. Another interaction is that the electron beam can ionize the atoms, and x-ray emitted, which depend on the elemental composition of the sample. Also, by scanning the surface of the sample and detecting the x-ray with another detector, chemical composition and their distributing over the sample which known as energy dispersive x-ray (EDX) could be analysed. Therefore, from the SEM we can obtain a magnification image of the surface of the sample as well as the chemical composition. The SEM imaging for the ZnO NPs and ZnO NRs are shown in Figure 4-3. The estimated average size of the ZnO NPs is  $\sim 80$  nm [52], while the diameter of the ZnO NRs estimated to be  $\sim 100$  nm [59].

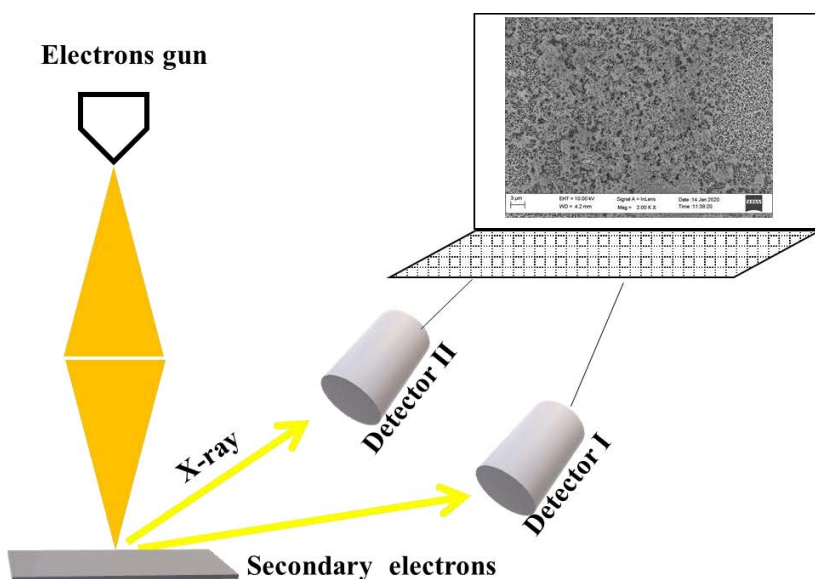


*Figure 4-2 Schematic diagram of the SEM.*

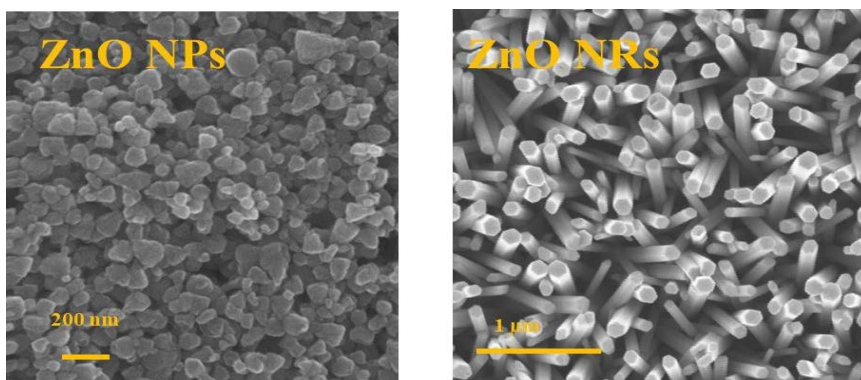


*Figure 4-3 SEM imaging of ZnO NPs (left), and ZnO NRs (right).*

#### **4.1.3 Transmission electron microscopy (TEM)**

The TEM was performed using double-corrected Linköping FEI Titan3 60–300, operated at 300 kV. The microscope is equipped with a monochromator with high brightness XFEG gun image, probe Cs correctors and solid angle Super-X EDX detector. The TEM measurement is quite similar to SEM, but it requires sample preparation to be in a very thin thickness ( $\sim 100\text{nm}$ ). Also, the TEM is composed of electron source, electromagnetic lenses, and electron detector. The sample should be fixed along the electron beam. The electron beam is accelerated and focused into the sample by lenses then transmitted through the sample. The transmitted beam is magnified and then detected. It is possible for the TEM to magnify images at the atomic resolution. Scanning TEM (STEM) can be measured by focusing the electrons beam into specific point of the sample and detecting the transmitted beam, and by scanning the surface of the sample we can view the magnified image of the sample as well as the chemical composition of the sample (EDX). Figure 4-4 shows the

principle operation of the TEM (left) and the TEM image of the synthesized ZnO/GR/Ag/AgI nanocomposite (right). We could see that there is a conjunction between the GR sheet and the nanocomposite, where the GR is functioning as a substructure for assembling the NPs besides being an electrical bridge between the nanocomposite during the photocatalytic reaction [52].

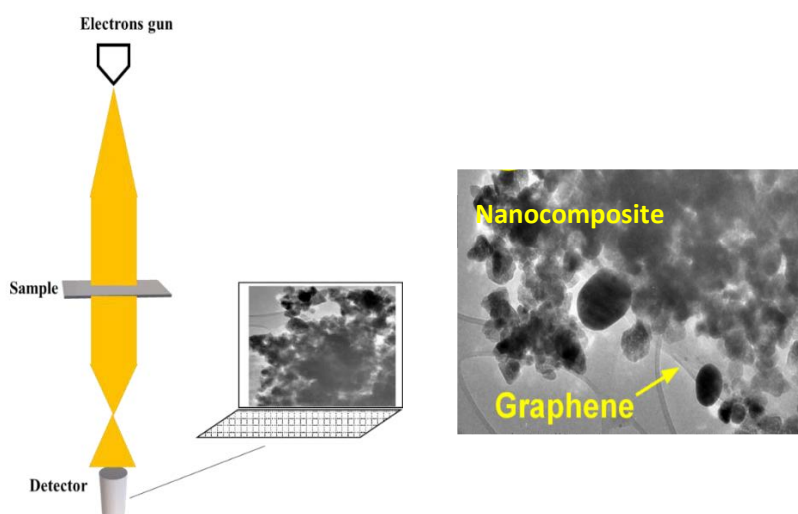


*Figure 4-4 Schematic diagram of TEM set up (left) and TEM image of the ZnO/GR/Ag/AgI nanocomposite (right).*

#### 4.1.4 X-ray photoelectron spectroscopy (XPS)

XPS (PHI 5600 mode) was used in this thesis to study the surface properties and the chemical composition of the synthesized ZnO nanocomposites. The XPS was calibrated using (C 1s) 284.6 eV as a reference for all binding energies. The theory behind the XPS is the photoelectric effect, where x-ray beam with specific photons energy ( $h\nu$ ) strike the nanocomposite surface at ultra-high vacuum conditions, then the photoelectrons are emitted at different kinetic energy ( $E_k$ ) where  $E_k = h\nu - E_b$  [79] as shown in Figure 4-5. Any element existence in the surface of the nanocomposites will produce an energy spectrum with certain binding energy according to their electronic structure [79]. From the spectrum and with a comparison of the XPS database the chemical composition of the nanocomposite can be determined. The spectrum of XPS scan survey of the ZnO/GR/Ag/AgI nanocomposite is presented in Figure 4-6. As can be seen, the presence of the Zn, O, C, Ag, and I elements in the ZnO/GR/Ag/AgI nanocomposite could be identified.

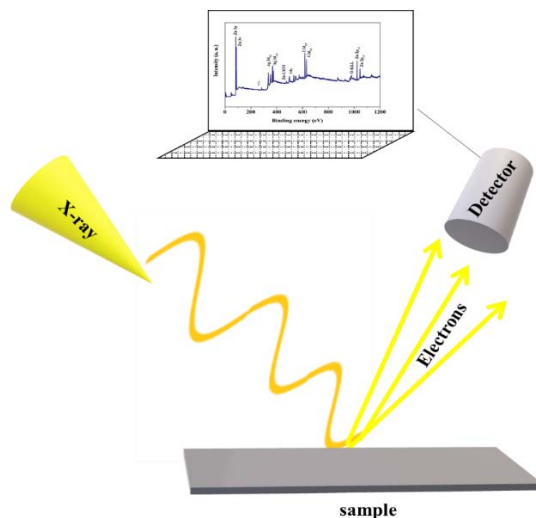


Figure 4-5 Schematic of the XPS principal

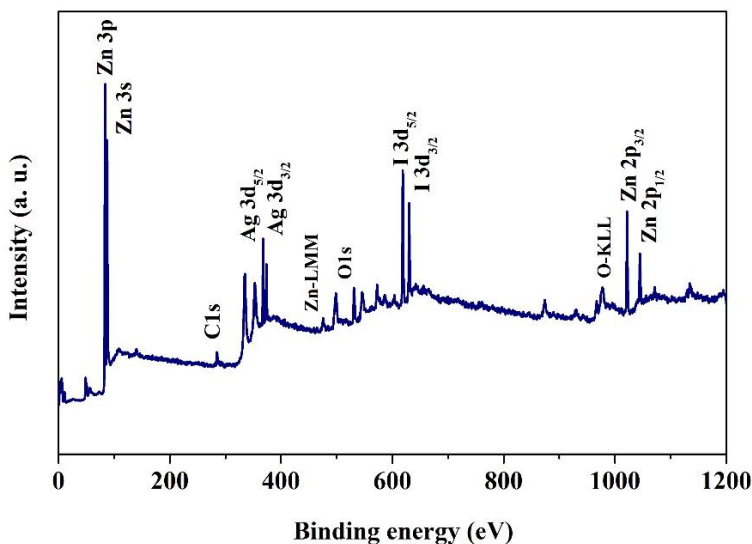


Figure 4-6 XPS scan survey of the ZnO/GR/Ag/AgI nanocomposite.

#### 4.1.5 UV-Vis spectroscopy

Light absorption properties were measured by Perkin Elmer Lambda 900 UV-Vis spectrophotometer DRS (JASCO, UV-550) in the wavelength range of 200–800 nm. It provides a double beam produced by Tungsten or Deuterium lamp, one of the beams goes through a reference medium for system calibration, whereas the other beam goes through the sample. The beam will be transmitted, then detected by a photodetector as explained in Figure 4-7. Finally, the absorption of the sample calculated and the absorbance spectrum of the sample versus the wavelengths will be plotted. The absorbance of the sample ( $A$ ) is calculated from the following equation:

$$A = \log \left[ \frac{I}{I_0} \right] \dots \dots \dots (4-3)$$

Where  $I$  is the light intensity transmitted through the sample,  $I_0$  is the intensity of the incident light.

The UV-Vis absorption spectrum of the synthesized ZnO NPs presented in Figure 4-8 Which shows that the ZnO NPs exhibit an absorption peak in the UV range at 366 nm.

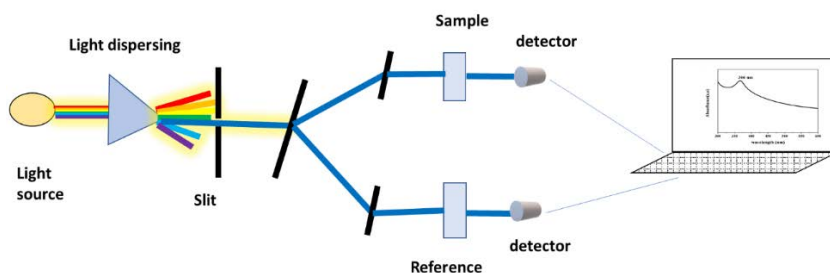


*Figure 4-7 Schematic of the UV-Vis absorption spectrometer.*

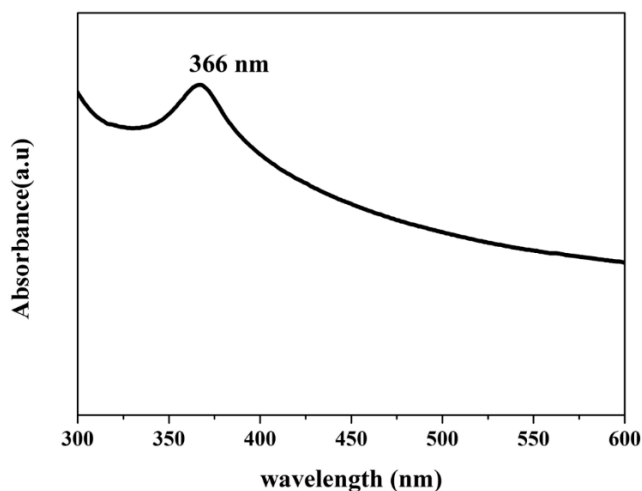


*Figure 4-8 The UV-Vis absorbance spectrum of the synthesis ZnO NPs.*

#### **4.1.6 Cathodoluminescence spectroscopy (CL)**

Optical characterization by cathodoluminescence (CL) using Gatan Mono CL4 system combined with Gemini LEO 1550 FE-SEM was obtained in this thesis. All CL measurements of the nanocomposites obtained at room temperature in the wavelength range of 200-800. In the CL measurements an electron beam (with several keV) attacks the sample at a very small focussing area, and the electrons are excited from the VB to the CB. Due to the recombination of the excited electrons and holes, electrons emit photons to be detected as illustrated in Figure 4-9, and the emission can be in a wide spectra range including ultraviolet, visible light and infrared. The CL image and CL spectrum of the ZnO NPs are presented in Figure 4-10. The spectrum shows a near band edge emission band beak at 376, and a broad emission which cover all the visible light wavelength band with beak at 614.



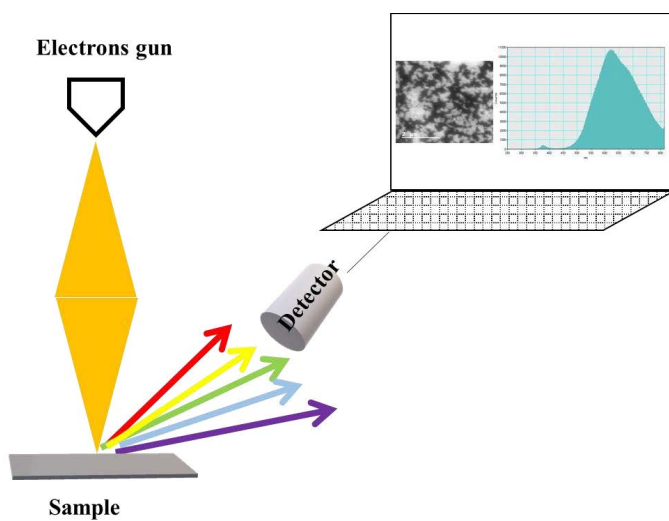


*Figure 4-9 Schematic diagram of the CL set up.*

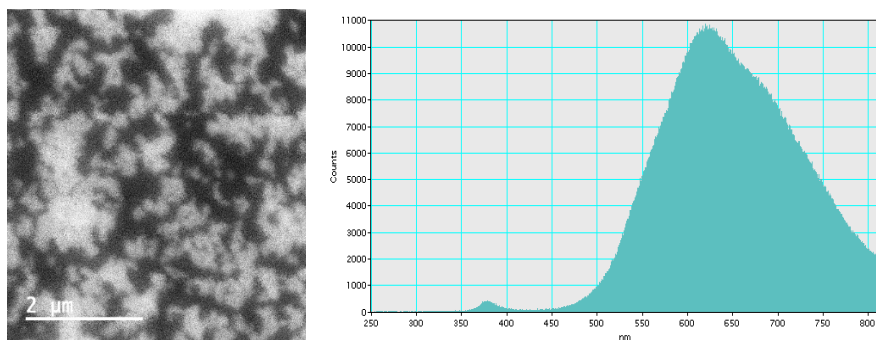


*Figure 4-10 Focusing area of the CL image (left), and CL spectrum of the ZnO NPs (right).*

## 4.2 Photodegradation set up

The photocatalytic experiments were performed using a solar simulator equipped with 100 W ozone free xenon lamp have a power of 1 sun (AM 1.5) to provide simulated solar light as presented in Figure 4-11. First, a 100 ml of the dye solution was mixed with an amount of 0.05 g catalyst and stirred for 30 min. under dark condition to reach the adsorption-desorption equilibrium between the dye and catalyst. Then a small amount of the mixture was withdrawn and centrifuged to separate the powder from the solution. After that the UV-Vis absorption spectrum was recorded for the separated solution. Then, the solar simulator was turned on, and with a specific time interval a small amount of the mixture was withdrawn, centrifuged and the UV-Vis absorption spectra were recorded.

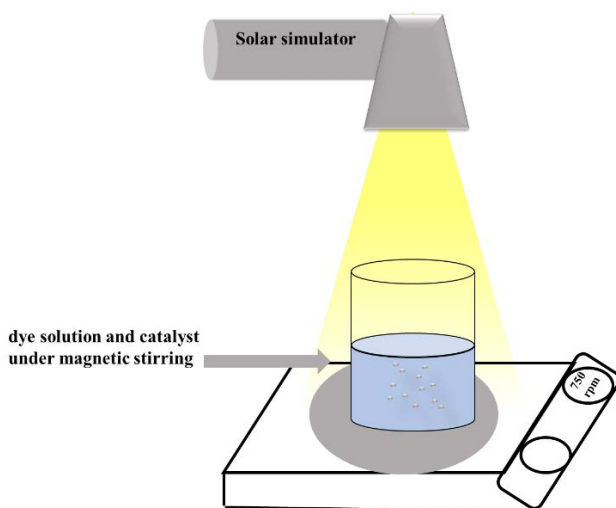


*Figure 4-11 Photodegradation experiment under solar light.*

### 4.3 Three Electrodes Set-up

The PEC activities of the synthesized photoelectrodes were studied using SP-200 potentiostat (Bio-Logic, Claix, France) with three electrodes setting as presented in Figure 4-12. A platinum (Pt) sheet and standard Ag/AgCl in 3 M KCl was applied as counter and a reference electrode, respectively. Whereas, the as synthesized photoelectrodes applied as working electrodes with a total area of the electrode immersed in the electrolyte of 1 cm<sup>2</sup>. Sodium sulfate (Na<sub>2</sub>SO<sub>4</sub>) with 0.1 M was used as an electrolyte for all the PEC measurements. Solar light was obtained from 100W ozone free xenon lamp in a solar simulator with an output power of 1 sun.

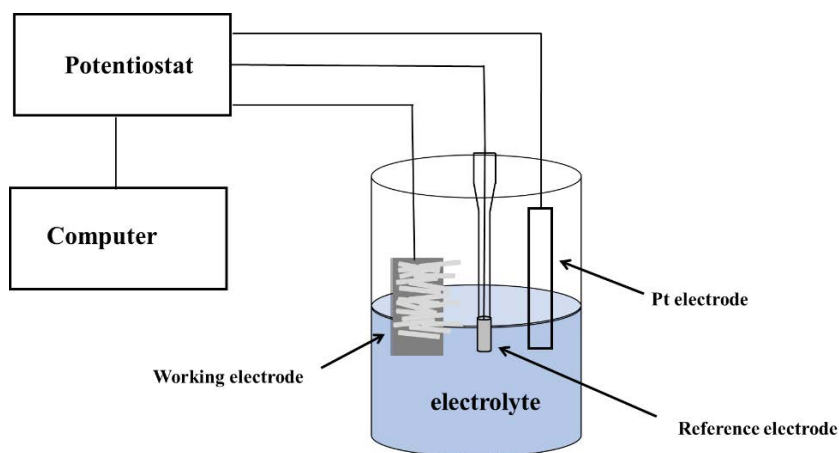


*Figure 4-12 PEC measurements with three electrode configurations*

## 5 Results and Findings

The result of the synthesis and characterization of some nanostructured materials based on ZnO NSs for visible light photo-processes are discussed based on five published papers and one manuscript. Also, some of the materials discussed in this thesis comes from my previous works attached to this thesis [20, 42, 52, 63, 67].

### 5.1 Photodegradation of Organic Dyes

#### 5.1.1 ZnO NPs

In this thesis, we started by exploring the photocatalysis performance of the ZnO NPs through the photodegradation of the CR dye under the illumination of solar light as published in paper I [20]. First, ZnO NPs were synthesized by the co-precipitation method at low temperature, the synthesized NPs were characterized by a variety of techniques. Finally, the photocatalysis activities were performed under different pH. The synthesized ZnO NPs have a quit well-distributed particles shape with an average of 100 nm in the size as estimated from the SEM imaging in Figure 5-1.

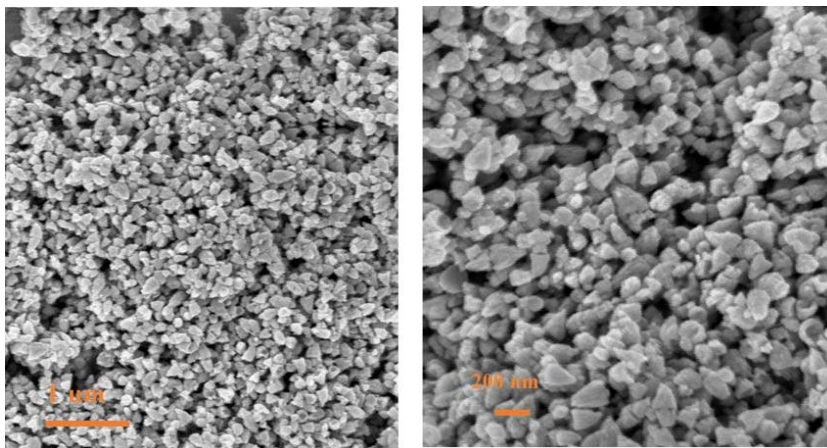


*Figure 5-1 FE-SEM images of ZnO NPs at two different magnifications.*

The optical properties of the ZnO NPs were obtained from the UV-Vis and CL measurements as shown in Figure 5-2 (a and b). From the UV-Vis spectrum, the ZnO NPs exhibited a maximum absorption peak at 366 nm. The optical band gap of the prepared ZnO NPs was found to be  $\sim 2.9$  eV which calculated from the Tauc's plot (see the intersect of Figure 5-2(a)) which is smaller than the band gap of the bulk ZnO. This could be ascribed to the native point defects on the ZnO NPs that occurred during the growth process of the ZnO NPs. This resulted in a shift of the absorption toward the visible light region and a better photocatalysis performance could be observed. The CL spectrum of the ZnO consists of ultraviolet emission peak at 376 nm and a broad peak centered at  $\sim 600$  nm as displayed in Figure 5-2 (b), which covers the whole visible light region. The broad beak could be attributed to the existence of intrinsic deep level emission of oxygen

interstitial ( $O_i$ ) and the presence of a hydroxyl group on the surface of the ZnO NPs [80–83].

The photocatalysis activities of the ZnO NPs were performed for the degradation of CR dye under the illumination of solar light at different conditions as presented in Figure 5-2 (c). When the CR irradiated with solar light without catalyst, no degradation was observed. When ZnO NPs were added to the CR solution without solar light, negligible degradation was observed. The photodegradation of the CR dye was obtained successfully when ZnO NPs were added under solar light illumination, where the concentration of the CR dye was reduced obviously. Although the ZnO is a wide band gap, it is observed that the ZnO NPs exhibit remarkable photocatalytic performance for the degradation of the CR dye under visible solar light. This performance is attributed to ( $O_2^-$ ) and ( $OH\cdot$ ) radicals. Also, the high redox potential, native points defects, and the unique nano-size are playing an important role in the photocatalysis performance.

The electrical properties of the ZnO NPs can be varied due to variation of the dye pH values [84] where the surface of the ZnO NPs could be negatively charged above zero point charge (9.0) and could be positively charged below the zero pint charge. Therefore, the photodegradation of the CR dye was studied for three different pH values (4, 7, and 10) and results for different pH values is presented in Figure 5-2 (d). Which shows the concentration of the CR dye during the photocatalysis reaction for 120 min. When the pH increased up to 10 better photocatalysis reaction was observed compared to the basic pH value of 7 and the degradation efficiency calculated to be 83 %. This is because, at high pH values, more  $OH^-$  ions are available to drive the photocatalytic reaction and produce  $OH\cdot$ , which is the main species responsible for the photocatalysis reaction. Thus the degradation efficiency was increased [25, 89]. The best degradation efficiency was found to be 85 % at the lower pH 4. We can observe

that the adsorption of the CR dye at pH 4 is higher where a photocatalytic reaction was observed in the dark which enhances the degradation efficiency. Moreover, anionic dyes such as CR can reach its maximum photodegradation efficiency at lower pH values. Because its surface will be negatively charged at lower pH value, which makes induced interaction with the positively charged ZnO NPs and increases the reaction rate. The positively charged NPs surface helps the movement of photogenerated electrons to react with the adsorbed  $O_2$  to produce  $O_2^{\cdot-}$  which is an active species in the photocatalytic reaction. In the end, higher degradation efficiency was obtained at pH 4. In addition to that from the radical scavenger experiment, it was found that  $O_2^{\cdot-}$  is the major species responsible for the photocatalytic reaction.

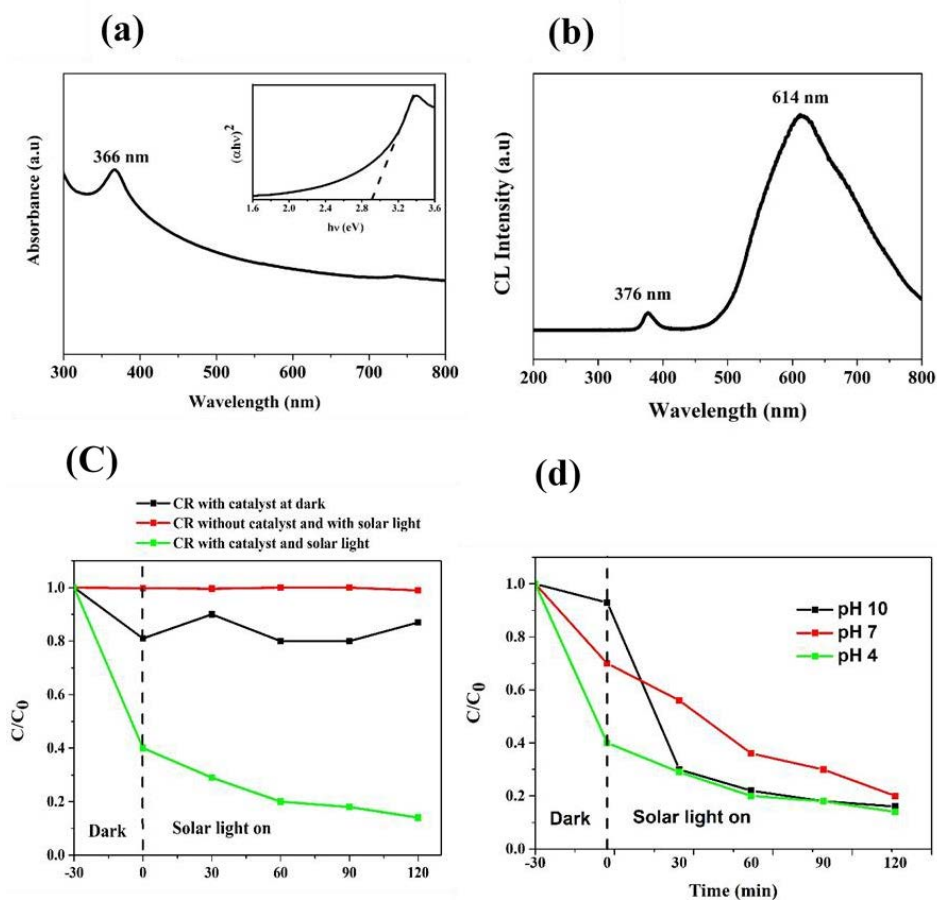


Figure 5-2 (a) UV-Vis spectrum of the synthesis ZnO NPS and the intersect shows the estimated optical band gap from Tauc's plot, (b) the CL spectrum of the synthesis ZnO NPs which dominated by two main beaks, (c) the photocatalysis performance at different condition.



### 5.1.2 Mg-doped ZnO NPs

To improve the photodegradation efficiency of ZnO NPs and its photo reactivities, Mg-doped ZnO NPs were investigated for photodegradation of MB dye as published in paper II [42]. Also, the low-temperature co-precipitation method was used to synthesized Mg-doped ZnO NPs with different Mg atomic concentrations relative to Zn (0, 3, 5, and 7 %). The synthesized Mg-doped ZnO NPs morphologies were seen by the FE-SEM imaging shown in Figure 5-3. We could see that more uniform size and morphology distribution of the ZnO NPs, than Mg-doped ZnO. The estimated average size was found to be ~ 58, ~67, ~90, and ~100 nm for the 0, 3, 5, and 7% samples, respectively. The size of the NPs was found to increase with increasing the doping concentration with an agglomeration of the particles. This is explained due to the increasing of the  $Mg^{2+}$  that were incorporated into ZnO crystal lattice which enhances the electron-hole separation and transfer during the photocatalytic reaction. The corresponding EDX spectrum was performed to study the Mg-content on the sample as shown in Figure5-4 for the 7% Mg-doped sample.

Furthermore, the incorporation of the Mg into the ZnO crystal lattice was confirmed by the XPS analysis as shown in Figure 5-4(a) for the 7 % sample. Figure 5-4(b) present the Zn 2p core-level spectrum which is divided into two peaks centered at 1022.3 and 1045.3 eV which indicates the presence of  $Zn^{2+}$ [86]. The Mg 2p XPS peak centered at 50.6 eV of the Mg-doped ZnO NPs is shown in Figure 5-4(c) which is attributed to the presence of  $Mg^{2+}$  that could replace the  $Zn^{2+}$  [87]. Figure 5-4(d) shows the O1s core level XPS spectra of 0% and 7% samples which decomposed into two Gaussian peaks. One peak at low binding energy centered at 530.97 and 530.99 eV for 0% and 7% Mg doping concentration, respectively. Which ascribe to the  $O_2^-$  ions of the wurtzite structure of the samples [20,87]. The higher binding energy peaks of 0% and 7% are centered at 531.31 and

532.09 eV, respectively is suggested to be related to H<sub>2</sub>O and O<sub>2</sub> [22, 92]. There is a slight shift towards higher binding energy for the 7% sample compared to the pristine ZnO NPs, which could be a sign of the Zn-O-Mg bond formation due to the substitution of Zn<sup>2+</sup> by Mg<sup>2+</sup> [89].

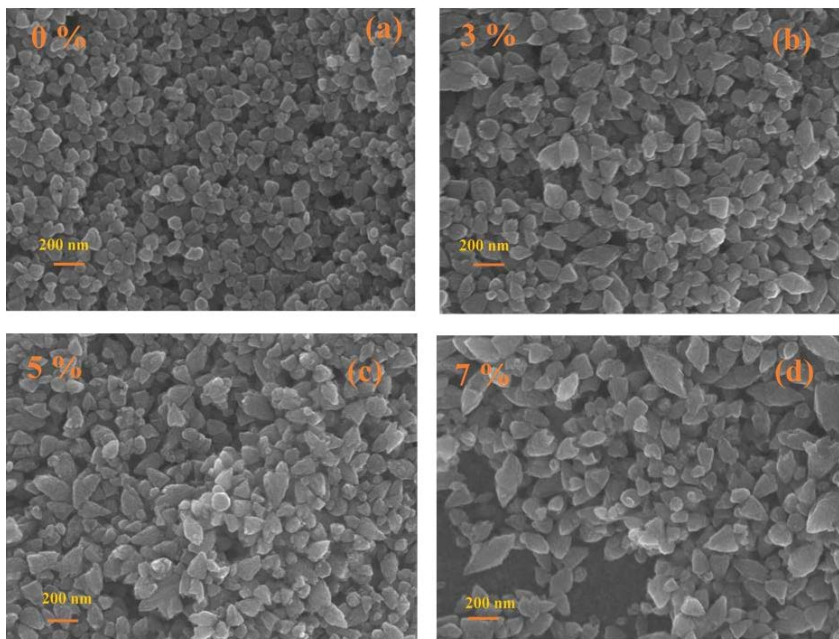


*Figure 5-3 FM-SEM images of the synthesized Mg-doped ZnO NPs with different Mg/Zn atomic concentration (a) 0 %, (b) 3 %, (c) 5 % and (d) 7 %.*

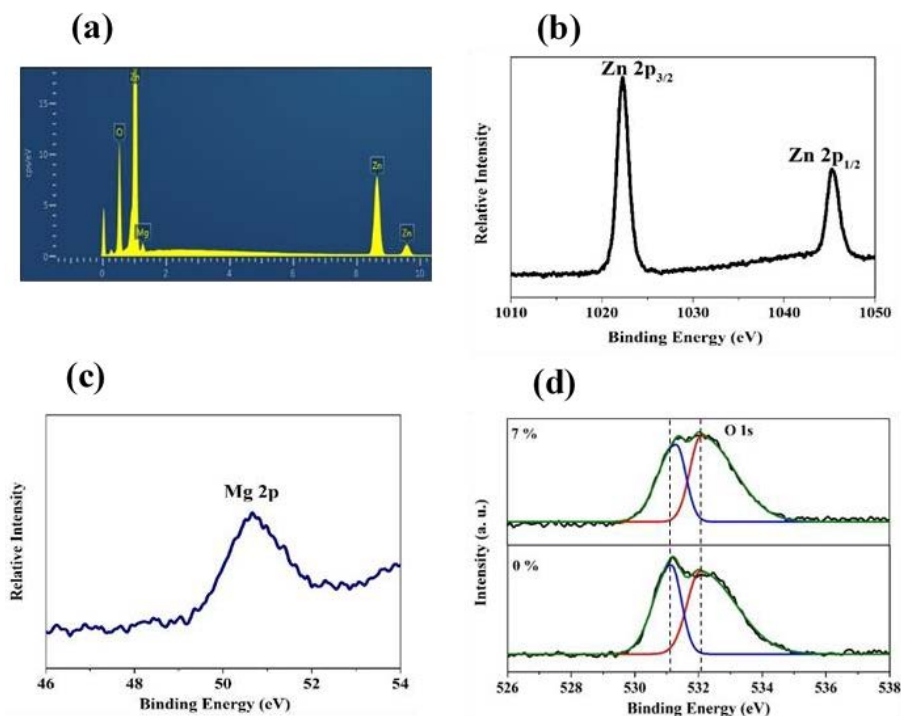
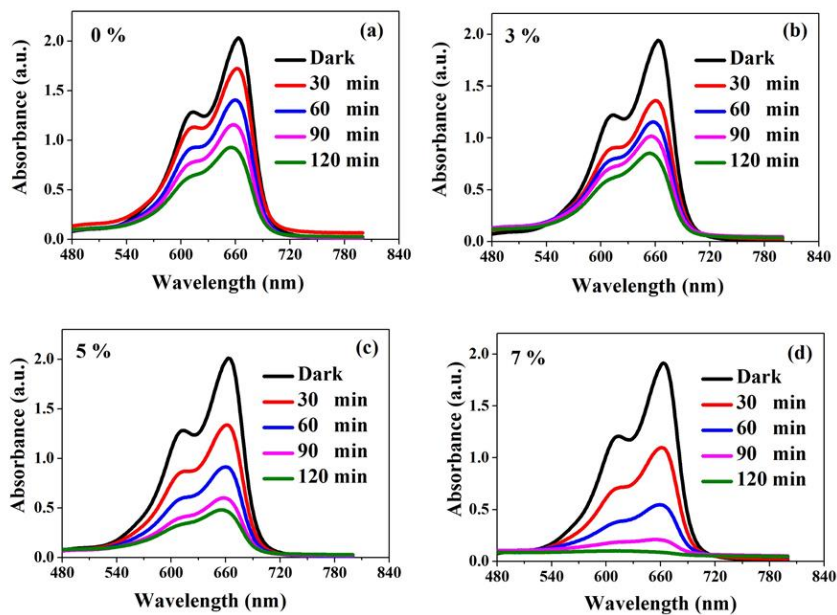


Figure 5-4 (a) EDX spectrum of 7% Mg-doped ZnO NPs and (b) XPS core level spectra of Zn 2p, (c) Mg 2p XPS core level spectra, and (d) O 1s XPS spectra of the ZnO NPs and Mg-doped ZnO NP.

The photodegradation efficiency result is presented in Figure 5-5 which shows the UV-Vis absorbance spectra of the MB for 0, 3, 5, and 7 % samples. The MB spectra exhibit the main beak centered at 663 nm, and its intensity decreases with time illumination for all samples which due to the degradation of the MB. The MB photodegradation efficiency (%) versus illumination time is shown in Figure 5-6. We could see that the photodegradation efficiency is improving with the addition of Mg doping concentration reaching 96 % for the 7 % sample. This could be attributed to the efficient substitution of the  $\text{Zn}^{2+}$  by the  $\text{Mg}^{2+}$  which enhances the photogenerated electron-hole pairs and, to the good absorption of hydroxyl

ions [90] which is an important species to drive the photocatalytic reaction as suggested by our previous study [42].



*Figure 5-5 Absorbance spectra of MB during photocatalytic activities for Mg-doped ZnO NPs (0, 3, 5, and 7%) under simulated solar light.*

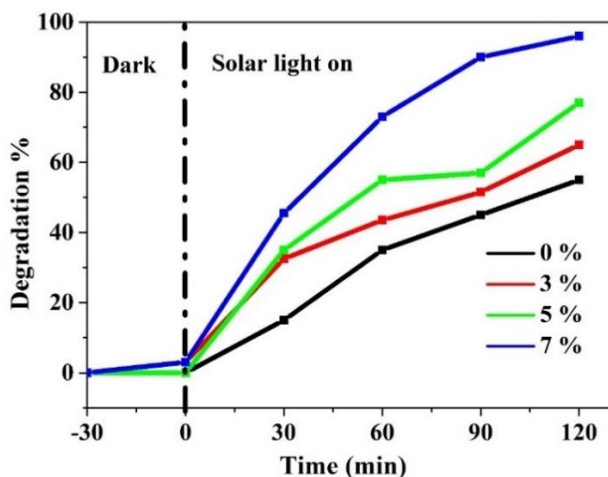
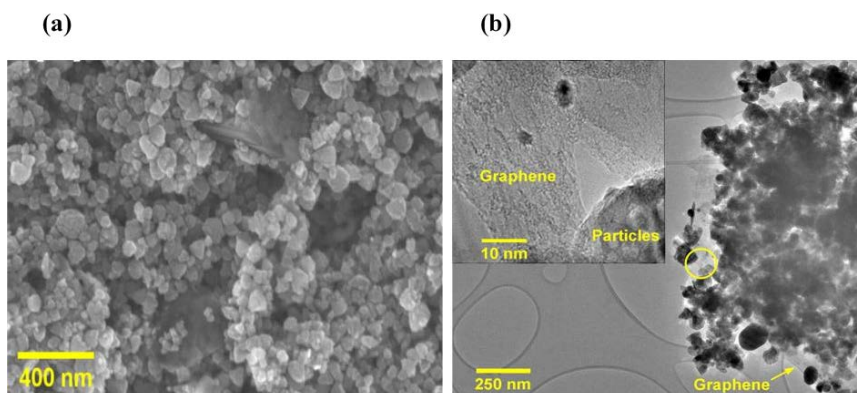


Figure 5-6 Photodegradation efficiency of MB for Mg-doped ZnO NPs (0, 3, 5, and 7 %) under simulated solar light.

### 5.1.3 ZnO/GR/Ag/AgI nanocomposite

The addition of the GR into the ZnO NPs can hinder the recombination of the electron-hole pairs in the photocatalysis reaction and enhances the separation and transportation process. Also, the deposition of the Ag/AgI nanoparticles can shift the absorption of light towards the visible range due to the lower band gap energy of the AgI and to the SPR effect from the Ag particles. The main purpose of this work is based on paper III which is to synthesis a new plasmonic ZnO/GR/Ag/AgI nanocomposite to enhance the photocatalysis activities under solar light. The blending of the AgI into the ZnO/GR/Ag/AgI nanocomposite with different AgI amounts (10, 20, and 30 %) was also studied. By low-temperature chemical methods combined with ultrasonic irradiation, we successfully obtained the ZnO/GR/Ag/AgI nanocomposite. The morphology of the nanocomposite was studied using SEM, and TEM as shown in Figure 5-7. The estimated average of the particles is  $\sim 100$  nm [52]. From the TEM image in Figure 5-7 (b) we can see the association of the NPs and the GR nano-

platelets in the ZnO/GR/Ag/AgI (20%) nanocomposite . Here the GR nanoplatelets are acting as a substructure to assemble the nanoparticles for electrons transfer.



*Figure 5-7 ZnO/GR/Ag/AgI (20%) nanocomposite. (a) the SEM image, and (b) The TEM and the inset shows a high magnification of the conjunction between GR and ZnO/Ag/AgI). The yellow circle in the main image is the location of the inset.*

For the elements existence and distribution confirmation in the ZnO/GR/Ag/AgI (20%) nanocomposite, STEM was studied and the result shown in Figure 5-8. Figure 5-8(a) is the STEM-HAADF imaging, and Figure 5-8(b-e) is the STEM-EDX elemental mapping which revealed that the nanocomposite is dominated by the ZnO, and the Ag/AgI NPs are localized in the nanocomposite. By comparing the mapping of Ag, and AgI we can notice that there is a dislocation in the Ag, which is attributed to the existence of two phases of Ag particles. One phase for the AgI and the other face could be belonging to the metallic Ag. The integrated EDX

spectrum shown in (f) confirmed the presence of Zn, O, Ag, and I elements in the ZnO/GR/Ag/AgI (20%) nanocomposite. The carbon mapping for the GR is not displayed due to the interference with the carbon support grid. From the elemental distribution in the ZnO/GR/Ag/AgI (20%) nanocomposite, we can expect a strong bond between the different counterpart in the nanocomposite, which can increase the efficiency of the electron-hole pairs generation and transportation during the photocatalysis process.

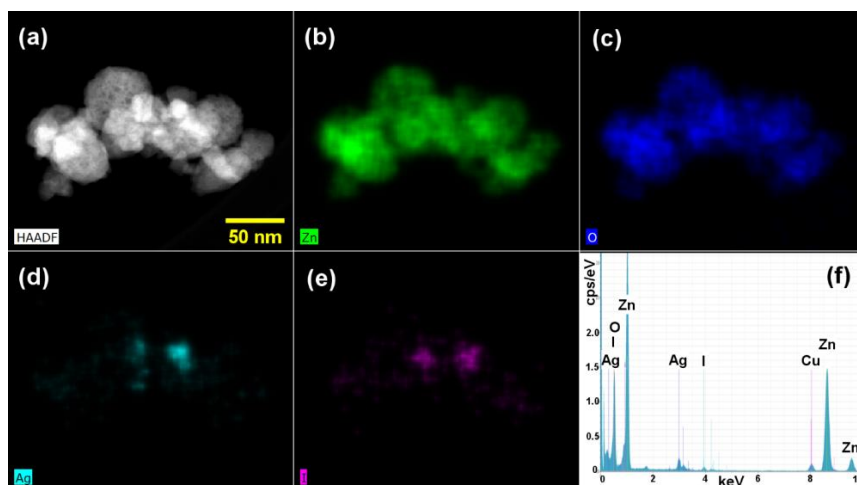


Figure 5-8 (a) STEM-HAADF image. (b-e) the STEM-EDX elemental mapping shows Zn, O, Ag, and I distributions, and (f) the integrated EDX spectrum for ZnO/GR/Ag/AgI (20%) nanocomposite.

The photodegradation efficiency of the CR dye was calculated for the ZnO, ZnO/GR, ZnO/Ag/AgI, and ZnO/GR/Ag/AgI nanocomposites with different amount of AgI after one hour of solar light and the result was shown in Figure 5-9. We could see that no degradation was observed for the CR dye in the absence of the nanocomposite (photolysis). This is an indication of the high stability of the CR under the simulated solar light.

The addition of GR, Ag/AgI to the ZnO NPs enhances the degradation efficiency significantly. The addition of the GR into the ZnO NPs increases the efficiency from 58% to 75% which is attributed to reduced recombination rate of photogenerated electron-hole pairs during the photocatalytic reaction. The main observation in the photocatalytic reaction is that loading the Ag/AgI into the ZnO/GR has further enhanced the degradation efficiency superiorly. As the loading of the AgI increased up to (20%) the highest degradation efficiency obtained is 90% after one hour of the photocatalytic reaction. This is ascribed to the shift of the absorption to the visible light range and to the SPR effect of the Ag particles. Interestingly, increasing the amount of the Ag/AgI up to 30%, the photodegradation efficiency dropped to 60%. This could be explained by the overloading of the Ag/AgI particles which may act as recombination centre. Also, the excess of the Ag/AgI particles could cover the active surfaces on the ZnO/GR/Ag/AgI (30%) nanocomposite hence reducing the charge separation efficiency. Therefore, the optimization of the Ag/AgI NPs loading is a crucial step for the synthesis of an efficient nanocomposite.



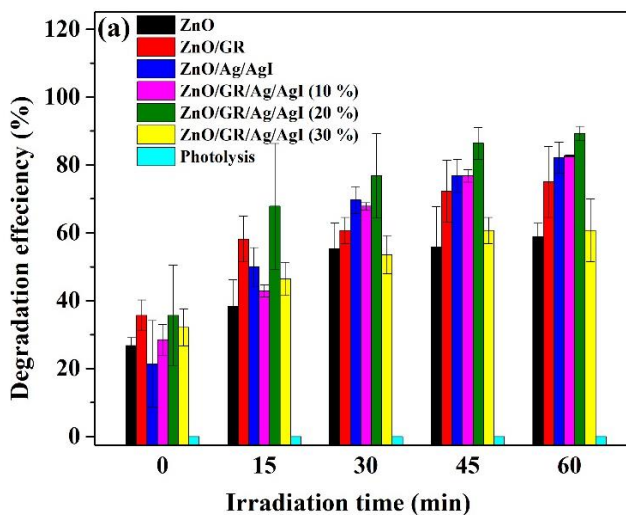


Figure 5-9 The photodegradation efficiency of CR dyes using ZnO, ZnO/GR, ZnO/Ag/AgI and ZnO/GR/Ag/AgI with different weight percentage of Ag/AgI.

## 5.2 ZnO-based photoelectrode for water oxidation

Due to its high photocatalytic performance for degradation of organic dyes, the ZnO nanocomposites were also explored for their ability in splitting water through PEC using water oxidation reaction under solar light in this thesis. First a ZnO photoelectrode was prepared by growing ZnO NRs on a conductive substrate using the hydrothermal chemical growth route at low temperature (90 °C) as discussed in section (2.4.2). Then different silver-based semiconductors such as  $\text{Ag}_2\text{CrO}_4$ ,  $\text{Ag}_2\text{WO}_4$ , and AgBr were deposited into the ZnO photoelectrodes using the SILAR method to produce different heterostructure electrodes for the PEC performance (see paper IV, V, and VI). Details on the result of each photoelectrode are discussed in the following sections.

### 5.2.1 ZnO/Ag<sub>2</sub>CrO<sub>4</sub> for enhanced visible-light PEC

Ag<sub>2</sub>CrO<sub>4</sub> is an efficient candidate to nanocomposite with ZnO NRs due to its narrow band gap (1.8 eV) which allows the absorption of the visible light and improves the PEC water oxidation for hydrogen evaluation. The deposition of Ag<sub>2</sub>CrO<sub>4</sub> onto the ZnO NRs will result in n-n heterojunction because both are n-type semiconductors. Thus, enhancement in the PEC water splitting will be achieved (paper IV). Different SILAR cycles for the deposition of the Ag<sub>2</sub>CrO<sub>4</sub> were performed and the corresponding photoelectrodes denoted as ZnO-Ag<sub>2</sub>CrO<sub>4</sub>-x (where x is the number of SILAR cycle).

The morphology of the ZnO NRs and ZnO-Ag<sub>2</sub>CrO<sub>4</sub>-8 photoelectrodes are shown in the FE-SEM image in Figure 5-10. Which shows the hexagonal structures of the ZnO NRs with a diameter of 100 nm estimated from Figure 5-10 (a). The deposition of the Ag<sub>2</sub>CrO<sub>4</sub> result in sphere-like nanoparticles with a diameter of ~200 nm dispersed on the surface and in between the ZnO NRs as shown in Figure 5-10 (b) for the ZnO-Ag<sub>2</sub>CrO<sub>4</sub>-8 photoelectrode.

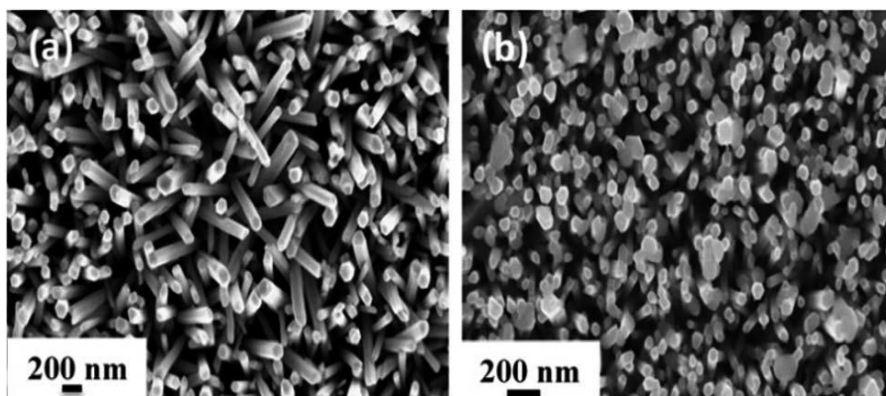


*Figure 5-10 the FE-SEM images of (a) ZnO NRs and (b) ZnO/Ag<sub>2</sub>CrO<sub>4</sub>-8 photoelectrodes.*

In order to investigate the absorption ability of the ZnO-Ag<sub>2</sub>CrO<sub>4</sub>-x photoelectrodes, the UV-Vis absorbance spectra and their relevant band gap calculation for the ZnO and ZnO-Ag<sub>2</sub>CrO<sub>4</sub>-x photoelectrodes are presented in Figure 5-11. As shown in Figure 5-11(a) the ZnO NRs exhibits the main absorption in the UV wavelength with very small absorption in the visible region due to its band gap energy. However, the ZnO-Ag<sub>2</sub>CrO<sub>4</sub>-x samples, exhibited a broad absorption in the visible light wavelengths due to the deposition of the Ag<sub>2</sub>CrO<sub>4</sub> particles which shift the absorption to the visible range. The corresponding band gap energy ( $E_g$ ) was calculated based on the theory and estimated from Tauc's plot which shows the plots of  $(\alpha h\nu)^2$  versus photon energy ( $h\nu$ ) presented in Figure 5-11(b). Where  $\alpha$  is the absorption coefficient,  $h$  is Planck's constant and  $\nu$  is the light frequency.

The optical band gap energy of the ZnO NRs photoelectrode decreased from 3.2 up to 1.9 eV after the deposition of the Ag<sub>2</sub>CrO<sub>4</sub> particles. Also, as the amount of the Ag<sub>2</sub>CrO<sub>4</sub> particles increases, the optical band gap decreases as well, and consequently enhanced visible light absorption of the ZnO-Ag<sub>2</sub>CrO<sub>4</sub>-x photoelectrodes is observed. This enhancement in the visible light absorption will allow a large amount of electron-hole pairs to be generated which improves the PEC performance under solar light.

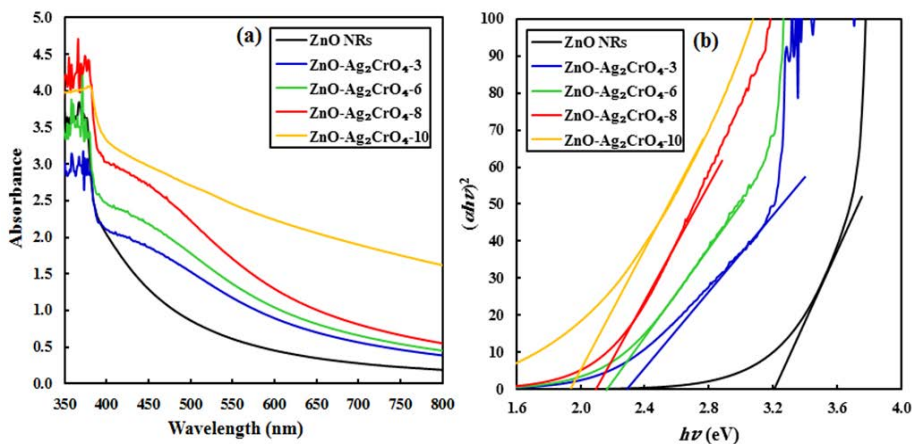


Figure 5-11 (a) UV-vis absorption spectra of the ZnO NRs and ZnO-Ag<sub>2</sub>CrO<sub>4</sub>-x photoelectrodes with different number of SILAR cycles. (b) the relevant plot of  $(ah\nu)^2$  versus  $h\nu$ .

The PEC water oxidation reaction is used to investigate the water splitting for hydrogen evaluation using the prepared ZnO NRs and ZnO-Ag<sub>2</sub>CrO<sub>4</sub>-x photoelectrodes, and the obtained PEC result is shown in Figure 5-12. The linear sweep voltammetry (LSV) curves were measured in dark and under solar light with potential from +0.0 to +1.4 V vs. Ag/AgCl electrode as presented in Figure 5-12(a). We could see that the ZnO NRs photoelectrode showed negligible photocurrent density under dark conditions, whereas the ZnO-Ag<sub>2</sub>CrO<sub>4</sub>-x photoelectrodes showed noticeable photocurrent density in the dark condition which indicates an enhancement in the electrical conductivity. When the LSV is measured under solar light, the conductivity of the ZnO NRs photoelectrode is slightly increased. But the ZnO-Ag<sub>2</sub>CrO<sub>4</sub>-x photoelectrodes showed a significant enhancement in the photocurrent density due to the deposition of the Ag<sub>2</sub>CrO<sub>4</sub> NPs which make a good electrocatalytic effect in the n-n heterojunction interface of the ZnO and Ag<sub>2</sub>CrO<sub>4</sub>. The new n-n heterojunction enhances the visible

light absorption which improves the photogeneration and transportation of the electron-hole pairs leading to higher photocurrent density. By increasing the amount of the  $\text{Ag}_2\text{CrO}_4$  NPs, the photocurrent density increases as well reaching  $2.51 \text{ mA.cm}^{-2}$  at a potential of 1.23 V versus Ag/AgCl with 8 SILAR cycles for the photoelectrode i.e.  $\text{ZnO-Ag}_2\text{CrO}_4$ -8 photoelectrode. By increasing the number of the SILAR cycles up to 10 times, the photocurrent density dropped down to  $0.91 \text{ mA.cm}^{-2}$  for the  $\text{ZnO-Ag}_2\text{CrO}_4$ -10 photoelectrode. The reason for this drop is the aggregation of excess  $\text{Ag}_2\text{CrO}_4$  NPs on the ZnO NRs surface, which destroyed the heterojunctions between the ZnO NRs and the  $\text{Ag}_2\text{CrO}_4$ . Also, the photo-response of the prepared photoelectrodes was measured at a potential of +0.5 V versus Ag/AgCl with turning the solar light on/off with a time interval of 20 s, and the result is presented in Figure 5-12(b). The photocurrent resulted from the  $\text{ZnO-Ag}_2\text{CrO}_4$ -x photoelectrodes is higher compared to the ZnO NRs photoelectrode which consistent with the LSV characteristics.

To study the effect of the amount of  $\text{Ag}_2\text{CrO}_4$  on the electronic proprieties of the photoelectrodes, the Mott–Schottky plots were analyzed at room temperature with a frequency of 3 kHz, and the  $V_{\text{FB}}$  of the ZnO NRs and  $\text{ZnO-Ag}_2\text{CrO}_4$ -x photoelectrodes was determined from Figure 5-12(c). The positive slopes of the ZnO NRs and  $\text{ZnO-Ag}_2\text{CrO}_4$ -x photoelectrodes indicating the n-type behavior of the ZnO NRs and  $\text{ZnO-Ag}_2\text{CrO}_4$ -x photoelectrodes with more larger slopes of  $\text{ZnO-Ag}_2\text{CrO}_4$ -x photoelectrodes compared to the bare ZnO NRs. This is attributed to the enhanced carrier concentration due to the construction of the n-n heterojunctions from the ZnO NRs and the  $\text{Ag}_2\text{CrO}_4$  NPs. In addition to that, a blue shift was observed in the  $V_{\text{FB}}$  values of the  $\text{ZnO-Ag}_2\text{CrO}_4$ -x photoelectrodes, compared to the potential of 0.49 V vs Ag/AgCl for the ZnO NRs. This is attributed

to the charge carrier concentration which changes in the n-n heterojunctions.

Moreover, from the IPCE curves (Figure 5-12(d)) of the ZnO NRs and ZnO-Ag<sub>2</sub>CrO<sub>4</sub>-8 photoelectrodes, we found that the ZnO NRs photoelectrode has a high photo respond at UV range wavelength ~375 nm. Whereas the ZnO-Ag<sub>2</sub>CrO<sub>4</sub>-8 photoelectrode shows better response at UV range wavelength in addition to the photo response in the visible-light region between 450–750 nm. The IPCE of the ZnO-Ag<sub>2</sub>CrO<sub>4</sub>-8 photoelectrode was found to be 40 % at 375 nm which increased by a factor of 1.5 compared to the ZnO NRs photoelectrode. Thus, the n-n heterojunctions of the ZnO-Ag<sub>2</sub>CrO<sub>4</sub>-8 photoelectrode photo generate and transfer chare carriers efficiently. More details on the mechanism behind the PEC performance with ZnO-Ag<sub>2</sub>CrO<sub>4</sub> n–n heterojunction presented in paper IV.

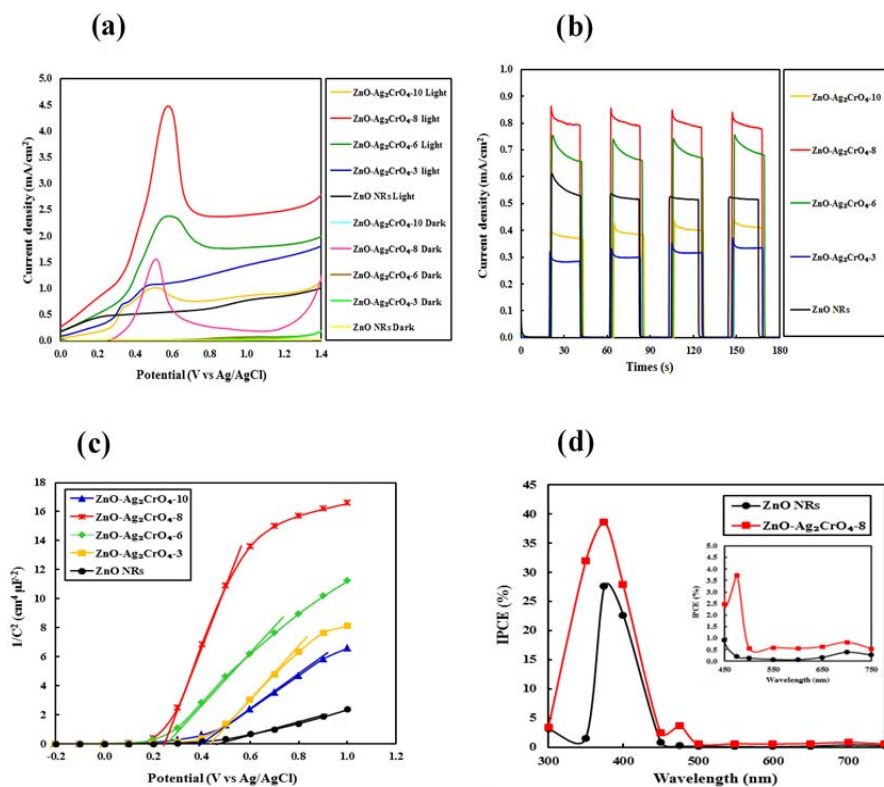


Figure 5-12 PEC performance for the ZnO NRs and ZnO-Ag<sub>2</sub>CrO<sub>4-x</sub> photoelectrodes (a) LSV curves under light and dark conditions, (b) The I-t curves under on/off solar light cycles, (c) Mott-Schottky plots at frequency of 3 kHz and (d) The plots of IPCE.

### **5.2.2 ZnO/Ag/Ag<sub>2</sub>WO<sub>4</sub> with plasmonic behaviour for enhanced PEC**

The ZnO/Ag/Ag<sub>2</sub>WO<sub>4</sub> photoelectrode was prepared as described in chapter 2, for the enhancement of the PEC water oxidation reaction (referring to paper V). the ZnO/Ag/Ag<sub>2</sub>WO<sub>4</sub> photoelectrode was synthesized through the low-temperature hydrothermal chemical growth followed by the SILAR method. The morphology of the ZnO/Ag/Ag<sub>2</sub>WO<sub>4</sub> photoelectrode is displayed in Figure 5-13(a) which clearly shows the deposition of the Ag/Ag<sub>2</sub>WO<sub>4</sub> particles on the vertically aligned hexagonal shape of the ZnO NRs. The size of the ZnO NRs is ~70 nm, and the Ag/Ag<sub>2</sub>WO<sub>4</sub> particle size varies between 30-150 nm. The structural properties of the ZnO/Ag/Ag<sub>2</sub>WO<sub>4</sub> were investigated by XRD and the result is shown in Figure 5-13 (b). This shows that ZnO, Ag, and Ag<sub>2</sub>WO<sub>4</sub> are present in the sample confirming the structure of the ZnO/Ag/Ag<sub>2</sub>WO<sub>4</sub> heterostructure. Additional confirmation of the ZnO/Ag/Ag<sub>2</sub>WO<sub>4</sub> heterostructure was found from the survey scan spectrum from the XPS measurement analysis, which confirms that the Zn, O, Ag and W elements are observed in the ZnO/Ag/Ag<sub>2</sub>WO<sub>4</sub> sample as shown in Figure 5-14.



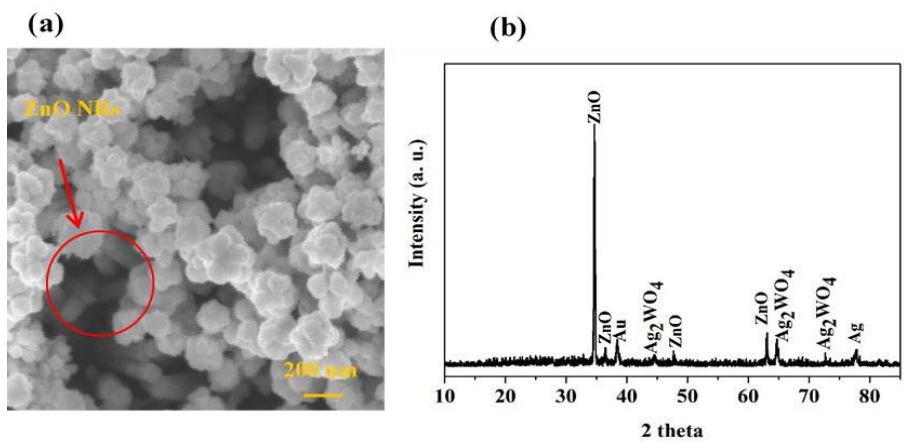


Figure 5-13 (a) SEM image and (b) XRD spectrum analysis of ZnO/Ag/Ag<sub>2</sub>WO<sub>4</sub> photoelectrode.

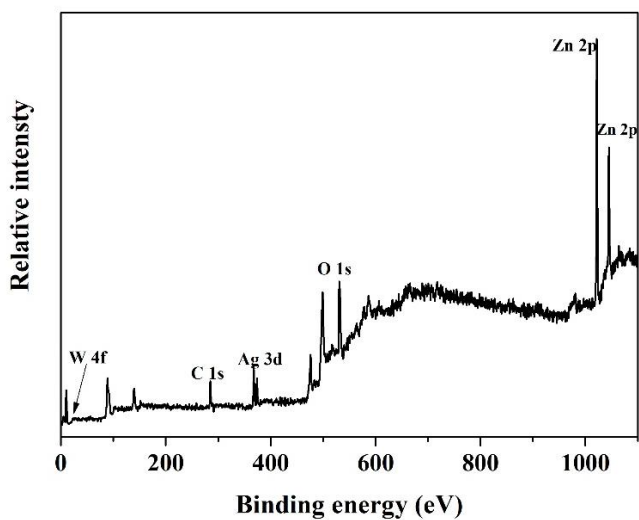


Figure 5-14 XPS spectrum of the ZnO ZnO/Ag/Ag<sub>2</sub>WO<sub>4</sub> photoelectrode.

The UV-Vis absorption spectra of the ZnO NRs and ZnO/Ag/Ag<sub>2</sub>WO<sub>4</sub> photoelectrodes were shown in Figure 5-15(a). Compared to the ZnO NRs photoelectrode, the ZnO/Ag/Ag<sub>2</sub>WO<sub>4</sub> exhibit a redshift in the visible light wavelength range. This shift is caused by the band gap engineering due to the deposition of the Ag<sub>2</sub>WO<sub>4</sub> particles and metallic silver which can induce the SPR effect, then enhances the PEC performance under visible light.

The PEC performance was investigated through the LSV, the photo-response, and the IPCE measurements. From the LSV curves in Figure 5-15(b), we can observe that under dark both electrodes show low and flat I-V curves, whereas under the solar light, a higher photoelectric conversion of the ZnO/Ag/Ag<sub>2</sub>WO<sub>4</sub> photoelectrode was observed with photocurrent density increased by factor three at the potential of 1.23 V (vs. Ag/AgCl) compared to the ZnO NRs photoelectrode. This enhancement was attributed to the efficient photogeneration and transportation of the electron-hole pairs due to the deposition of the Ag/Ag<sub>2</sub>WO<sub>4</sub> NPs on the surface of the ZnO NRs and to the SPR effect which increases the absorption of visible light. The result of that efficient ZnO/Ag/Ag<sub>2</sub>WO<sub>4</sub> photoelectrode for water oxidation was obtained [63, 95, 96]. In order to study the effect of the amount of the Ag/Ag<sub>2</sub>WO<sub>4</sub> NPs on the PEC performance, the photo-response was measured for the ZnO/Ag/Ag<sub>2</sub>WO<sub>4</sub> photoelectrodes with different SILAR cycles (5, 10 and 15 times). From the chronoamperometry measurements, the photocurrent density was recorded under on/off solar irradiation with a time interval of 20 s and applied potential of +0.5V as illustrated in Figure 5-15(c). As the SILAR cycle is increased up to 10 times higher photocurrent density was obtained which is increased by factor 2.5 compared to the photocurrent density achieved from the ZnO NRs photoelectrode. This result indicates that the

ZnO/Ag/Ag<sub>2</sub>WO<sub>4</sub> (10 times) photoelectrode has a high transient photocurrent response with good stability during the on/off light cycles. However, further increasing the SILAR cycle deposition of the Ag/Ag<sub>2</sub>WO<sub>4</sub> into the ZnO NRs up to 15 times, a reduction in the photocurrent density was observed. This is resulted from the formation of larger aggregates around the ZnO NRs due to the high amount of the Ag/Ag<sub>2</sub>WO<sub>4</sub>. Larger aggregates of the Ag/Ag<sub>2</sub>WO<sub>4</sub> can cover the active sites of the ZnO and cause junction destruction, which results in lower photoinduced charge carriers.

For an additional investigation of the ZnO/Ag/Ag<sub>2</sub>WO<sub>4</sub> (10 times) photoelectrode ability on the PEC reaction and water oxidation, IPCE curves of the ZnO NRs, and ZnO/Ag/Ag<sub>2</sub>WO<sub>4</sub> photoelectrodes were obtained as shown in Figure 5-15(d). It can be observed that the ZnO NRs photoelectrode shows high PEC activities in the UV region, with some weak performance in the visible light region. Whereas, the ZnO/Ag/Ag<sub>2</sub>WO<sub>4</sub> photoelectrode, shows an extension of the photoreactivity in the UV region as well as in the visible light region between 400 to 450 which is consistent with the UV-Vis result in Figure 5-15(a). The IPCE at the wavelength ~400 nm was found to be 20 and 30 % for ZnO NRs and ZnO/Ag/Ag<sub>2</sub>WO<sub>4</sub>, respectively. Which suggested to be due to the extended absorption region of the light and to the SPR effect of silver particles which enhances the electrons transfer between the ZnO and Ag<sub>2</sub>WO<sub>4</sub> during the redox reactions for H<sub>2</sub> and O<sub>2</sub> evaluation [63, 97].

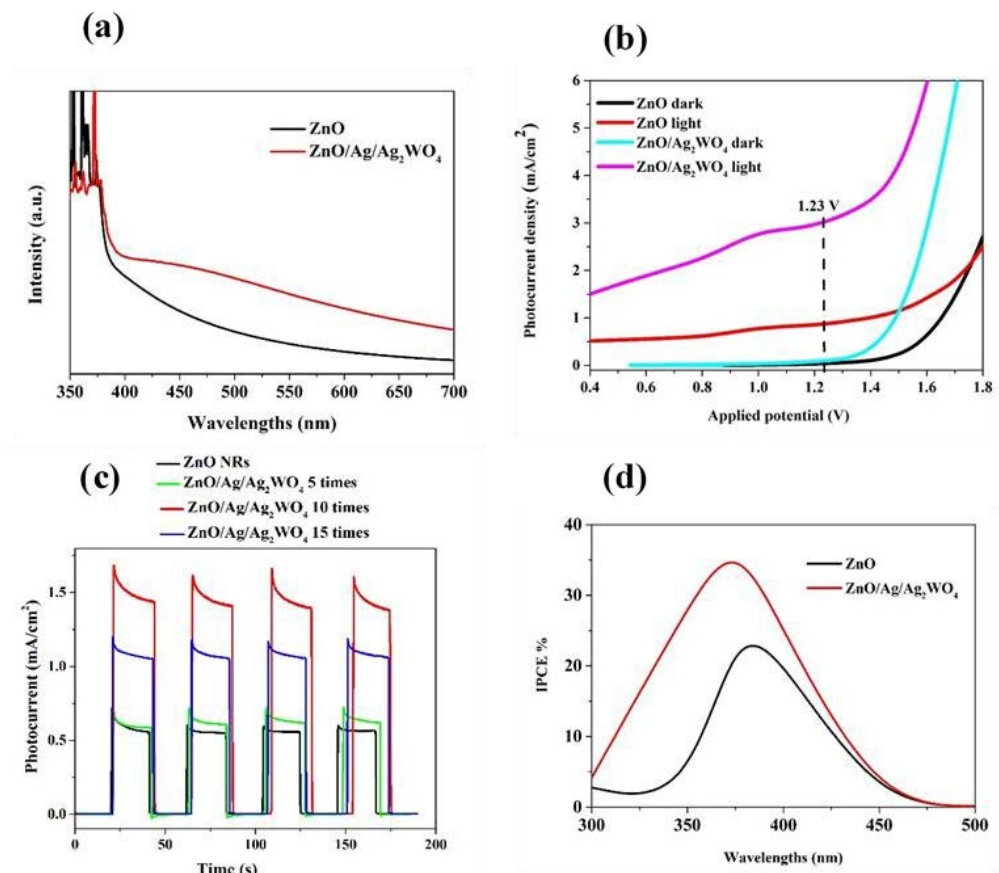


Figure 5-15 (a) The UV-vis absorption spectra of the ZnO NRs and the ZnO/Ag/Ag<sub>2</sub>WO<sub>4</sub> heterostructure., (b) LSV curves under light and dark conditions, (c) The I-t curves with solar light on/off cycles and (d) The plots of IPCE versus wavelength, for the ZnO NRs and ZnO/Ag/Ag<sub>2</sub>WO<sub>4</sub> photoelectrodes.

### 5.2.3 ZnO/Ag<sub>2</sub>WO<sub>4</sub>/AgBr

Although the deposition of the Ag<sub>2</sub>WO<sub>4</sub> into the ZnO NRs resulted in an efficient ZnO/Ag/Ag<sub>2</sub>WO<sub>4</sub> photoelectrode for water oxidation, still its bandgap is relatively large and some of the visible light regions was not utilized sufficiently. Therefore, lower band gap semiconductors mainly AgBr can be deposit into the ZnO/Ag/Ag<sub>2</sub>WO<sub>4</sub> photoelectrode to provide an absorption in the visible light region of the solar spectrum, which further enhances the PEC reaction. First, the ZnO NRs were grown on FTO substrates containing the seed layer of ZnO NPs using the low temperature aqueous chemical growth. Then Ag<sub>2</sub>WO<sub>4</sub> was deposited on the surface of the as-prepared ZnO NRs using the SILAR method followed by hydrothermal treatment by ion exchange of Ag<sub>2</sub>WO<sub>4</sub> into AgBr (more details on the photoelectrode preparation method is discussed in paper VI). It is worth to note that Ag particles might be introduced during sample preparation. But also, it is possible for Ag to be produced during the irradiation of the visible solar light due to the photoreduction of the AgBr during the course of the PEC reaction.

The EF-SEM imaging of ZnO/Ag<sub>2</sub>WO<sub>4</sub> and ZnO/Ag<sub>2</sub>WO<sub>4</sub>/AgBr photoelectrodes are shown in Figure 5-16 which shows the deposition of the Ag<sub>2</sub>WO<sub>4</sub>/AgBr particles on the ZnO NRs. We could observe that bigger particle sizes displayed for ZnO/Ag<sub>2</sub>WO<sub>4</sub>/AgBr photoelectrode compared to the ZnO/Ag<sub>2</sub>WO<sub>4</sub> photoelectrode with semi-crystal structure due to the effect of the AgBr. Also, very small particles can be identified, which could be due to different counterpart deposited into the ZnO NRs including Ag particles that might be produced during the sample preparation.

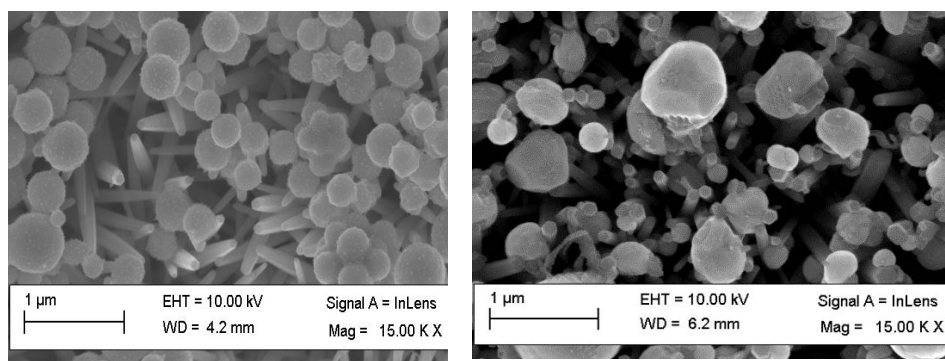


Figure 5-16 SEM Images of the  $\text{ZnO}/\text{Ag}_2\text{WO}_4$  (right) and (b)  $\text{ZnO}/\text{Ag}_2\text{WO}_4/\text{AgBr}$  (left) heterostructure.

From the UV-Vis absorption spectra in Figure 5-18(a), a redshift was observed in the visible light wavelengths range for the  $\text{ZnO}/\text{Ag}_2\text{WO}_4/\text{AgBr}$  photoelectrodes. Also, the band gap energy was reduced from 3.2 to 3.14 eV, which found from the plots of  $(\alpha h\nu)^2$  versus photon energy ( $h\nu$ ) as shown in Figure 5-18(b). The improvement in the absorption ability on the  $\text{ZnO}/\text{Ag}_2\text{WO}_4/\text{AgBr}$  heterostructure can be attributed to the deposition of the AgBr due to its lower band gap energy compared to the ZnO band gap energy. Higher absorption ability in the heterostructure are beneficial for increasing the PEC reaction efficiency.

The PEC activity of the photoelectrodes were investigated by the LSV measurement in the dark and under solar light conditions at the potential of 1.23 V (vs. Ag/AgCl) electrode. From the dark scans, a negligible photocurrent density of the ZnO NRs photoelectrode was observed, which implies a good surface quality of the ZnO NRs as shown in Figure 5-18(c). Compared with the ZnO photoelectrode, the  $\text{ZnO}/\text{Ag}_2\text{WO}_4$ , and  $\text{ZnO}/\text{Ag}_2\text{WO}_4/\text{AgBr}$  photoelectrodes showed a small photocurrent den-

sity in the dark measured of 0.01, and 0.015 mA.cm<sup>2</sup>, respectively indicating an improvement in the electrical conductivity. When solar light is on, lower photocurrent was observed for the ZnO, whereas the photocurrent density is highly increased for the ZnO/Ag<sub>2</sub>WO<sub>4</sub>, and ZnO/Ag<sub>2</sub>WO<sub>4</sub>/AgBr photoelectrodes with an optimal photoelectric conversion for the ZnO/Ag<sub>2</sub>WO<sub>4</sub>/AgBr photoelectrode. The remarkably enhanced photocurrent density of the ZnO/Ag<sub>2</sub>WO<sub>4</sub>/AgBr photoelectrode is due to the heterojunction effect upon deposition of the Ag<sub>2</sub>WO<sub>4</sub> and the AgBr NPs into the surface of the ZnO NRs. Which is an indication of a high density of the photogenerated electrons that can be transferred from the ZnO/Ag<sub>2</sub>WO<sub>4</sub>/AgBr photoelectrode to the counter electrode providing higher photocurrent. This is attributed to the enhanced charge carrier separation and transportation efficiency and due to the high absorption of the solar light and the shift of the absorption into the visible light range. The photo-response of the synthesized photoelectrodes was studied using the chronoamperometry measurements where the photocurrent density with on/off solar light each 20 s was recorded with an applied potential of +0.5V as shown in Figure 5-18(d). The photocurrent densities were found to be 0.6, 2, and 2.3 mA/cm<sup>2</sup>, for the ZnO NRs, ZnO/Ag<sub>2</sub>WO<sub>4</sub>, and ZnO/Ag<sub>2</sub>WO<sub>4</sub>/AgBr photoelectrodes, respectively. Consistent with the LSV analysis, the photocurrent density of the ZnO/Ag<sub>2</sub>WO<sub>4</sub>/AgBr photoelectrode remained the optimal photoelectrode with a higher response under solar light. The great enhanced PEC activities of the ZnO/Ag<sub>2</sub>WO<sub>4</sub>/AgBr photoelectrodes could be attributed to the effectively enhanced photo-response and good electrons transfer to acquire the redox reaction [94]. The energy band position of the ZnO/Ag<sub>2</sub>WO<sub>4</sub>/AgBr heterojunction with possible electron transfer path is illustrated in Figure 5-17. Light with lower energy photons will excite electrons from the VB to the CB of the AgBr due to its suitable band gap (~2.6 eV), whereas, higher

energy photons can excite electrons in the ZnO and in the  $\text{Ag}_2\text{WO}_4$  semiconductors. Rapid electrons transfer can take place quickly where electrons are transferred from the CB of the AgBr to the CB of the ZnO and  $\text{Ag}_2\text{WO}_4$  consequently. Then electrons will be transferred to the photoelectrode contact for reduction reaction in the Pt electrode site where  $\text{H}_2$  can be released. Holes which left in the VB will perform oxidation reaction and  $\text{O}_2$  could be released. The efficient electrons transfer between the heterojunction can reduce the recombination rate and enhances the photocatalytic reaction.



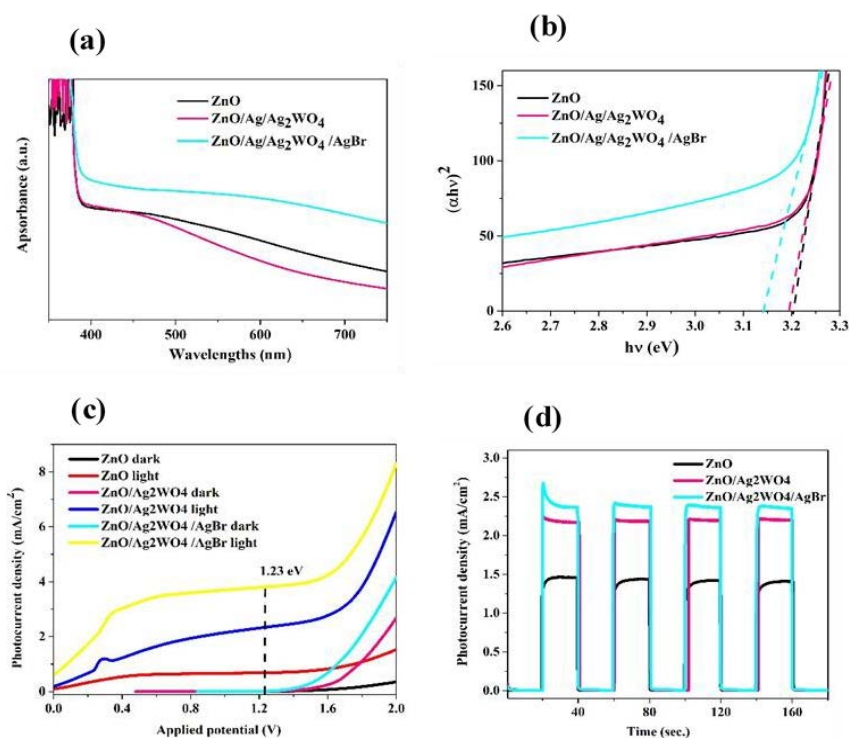


Figure 5-18 (a) UV-vis absorbance spectra (b) the plots of  $(\alpha h\nu)^2$  versus  $h\nu$ . (c) LSV curves under light and dark conditions and (d) The I-t curves with solar light on/off cycles of the ZnO NRs, ZnO/Ag<sub>2</sub>WO<sub>4</sub> and ZnO/Ag<sub>2</sub>WO<sub>4</sub>/AgBr photoelectrodes.

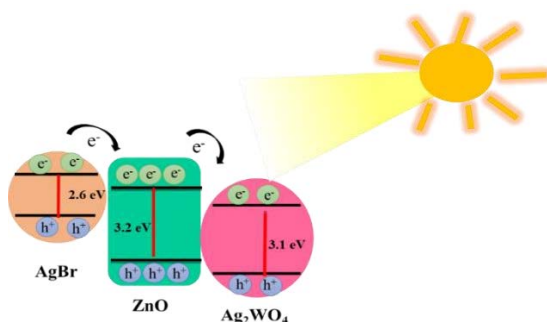


Figure 5-17 Possible electrons transfer in the ZnO/Ag<sub>2</sub>WO<sub>4</sub>/AgBr heterojunction.

## 6 Conclusion and Future work

### 6.1 Conclusion

In this thesis, ZnO with different nanocomposites was synthesized using the low-temperature growth methods for visible light-driven photo processes. Two photo processes were investigated in this research work (1) photocatalytic degradation of organic pollutants and (2) PEC water splitting. In Paper I, II, and III the photodegradation of organic dyes were investigated using different nanocomposites, whereas the photocatalytic water splitting using different photoelectrodes was discussed in paper IV, V, and VI.

In paper I, the synthesis of the ZnO NPs using the co-precipitation method at 60 °C for photodegradation of the CR Dye at different pH values was studied. The photocatalytic activities were explored at different conditions, and the ZnO NPs showed higher photodegradation efficiency of the CR dye at lower pH 4. This is due to the high adsorption of the CR dye, and to the induced interaction between the positively charged ZnO NPs and the negatively charged CR dye at lower pH which helps the migration of photoinduced electrons to drive the photocatalytic reaction.

In Paper II Mg-doped ZnO NPs with different Mg atomic concentrations relative to Zn (0, 3, 5, and 7 %) were synthesized and their photocatalytic performance for the degradation of MB dye was investigated. It was found that the size of the ZnO NPs is increasing with the increment of doping concentration and higher photocatalytic performance was achieved with 7 % doping concentration. This result was explained by the increasing incorporation of the  $\text{Mg}^{2+}$  into the ZnO crystal lattice which, enhances the electron-hole separation and transfer during the photocatalytic reaction.

In paper III a new plasmonic ZnO/GR/Ag/AgI nanocomposite to enhance the photocatalysis performance was investigated. Also, the blending of the AgI into the ZnO/GR/Ag/AgI nanocomposite with different AgI amounts (10, 20, and 30 %) was studied for degradation of CR dye. The ZnO/GR/Ag/AgI nanocomposite was obtained using the low-temperature chemical method combined with ultrasonic irradiation. The characterization techniques confirmed that the ZnO/GR/Ag/AgI nanocomposite was successfully obtained, and the photocatalytic efficiencies increased with increasing the blending of AgI up to 20 % which is found to be 90 %. This result is attributed to the shift of the absorption to the visible light range and to the SPR effect of the Ag particles that might be introduced into the nanocomposite during the sample preparation. Interestingly, increasing the AgI amount up to 30 % dropped the photocatalytic efficiency to 60%. This reduction was ascribed to a high amount of the AgI loaded into the nanocomposite which covered the active surfaces of the nanocomposite which is then reduced the electron-hole separation efficiency.

For the second photo-process, ZnO photoelectrode composite with different silver-based semiconductors for new heterojunctions structures to enhance the PEC performance for water splitting. First ZnO photoelectrode was prepared by the growth of the ZnO NRs on a conductive substrate using the hydrothermal chemical growth route at low 90 °C. Then  $\text{Ag}_2\text{CrO}_4$ ,  $\text{Ag}_2\text{WO}_4$ , and AgBr were deposited into the ZnO photoelectrodes using the SILAR method. In paper IV  $\text{Ag}_2\text{CrO}_4$  deposited onto the ZnO NRs using different SILAR cycles and ZnO- $\text{Ag}_2\text{CrO}_4$  n-n heterojunction was produced. Higher PEC performance was achieved with ZnO- $\text{Ag}_2\text{CrO}_4$ -8 photoelectrode. The higher PEC performance is attributed to the increase of the visible light absorption and the reduction of the bandgap after deposition of the  $\text{Ag}_2\text{CrO}_4$ , which increases the number of

electron-hole pairs to be generated which improves the PEC performance under solar light. Further increase in the SILAR cycles resulted in a reduction in the PEC performance due to the aggregation of excess  $\text{Ag}_2\text{CrO}_4$  NPs on the ZnO NRs surface, which results in the heterojunction destruction between the ZnO NRs and the  $\text{Ag}_2\text{CrO}_4$ .

In Paper IV  $\text{Ag}_2\text{WO}_4$  deposited into the ZnO NRs and ZnO/Ag/ $\text{Ag}_2\text{WO}_4$  photoelectrodes were produced and their PEC performance was investigated. Higher PEC efficiency was obtained from the ZnO/Ag/ $\text{Ag}_2\text{WO}_4$  photoelectrode with 10 times SILAR cycle compared to the ZnO NRs photoelectrode. This enhancement was attributed to the efficient photogeneration and transportation of the electron-hole pairs in the heterojunction and to the SPR effect of the silver particles. In order to further enhance the absorption of visible light in the ZnO/Ag/ $\text{Ag}_2\text{WO}_4$  photoelectrode, AgBr deposited over the ZnO/Ag/ $\text{Ag}_2\text{WO}_4$  photoelectrode and their PEC ability was studied in paper VI. Compared to the ZnO photoelectrode and ZnO/ $\text{Ag}_2\text{WO}_4$  photoelectrode, The ZnO/ $\text{Ag}_2\text{WO}_4$ /AgBr photoelectrode showed higher PEC performance due to the heterojunction effect upon deposition of the  $\text{Ag}_2\text{WO}_4$  and the AgBr NPs into the surface of the ZnO NRs. This deposition provides a high density of the photogenerated electrons that can be transferred for the oxidation reaction due to the absorption of the visible light wavelengths.

Therefore, the combination of different nanomaterials to form new nanocomposites with new properties for photocatalytic processes were successfully obtained. The new nanocomposites exhibited a synergetic effect due to the combination of the properties of all the counterparts of the nanocomposite.

## 6.2 Future Work

For future work to accomplish the present work, there are some issues which have to be studied. Regarding the silver-based photoelectrode, it was discussed that metallic silver was produced in the photoelectrode which produces the SPR effect during the photocatalytic reaction. Therefore, confirmation of the metallic silver on the substrate and their size using high-resolution TEM is required for the photoelectrode before and after the photocatalytic reaction. Also, the durability and stability of the photoelectrodes are essential for the long-term sustainability of the prepared photoelectrodes. A stability test can be performed by investigating a long-term photo-response of the photoelectrode by measuring the photocurrent density of the electrode versus time. Moreover,  $H_2$  evaluation must be analysed by measuring the amount of hydrogen that could be released during the PEC reaction, which is planned to be done using the  $ZnOAg_2CrO_4$ , the  $ZnO/Ag_2WO_4$  and the  $ZnO/Ag_2WO_4/AgBr$  photoelectrodes.

## 7 References

- [1] M. Ge, J. Cai, J. Iocozzia, C. Cao, J. Huang, X. Zhang, J. Shen, S. Wang, S. Zhang, K.-Q. Zhang, Y. Lai, Z. Lin, A review of TiO<sub>2</sub> nanostructured catalysts for sustainable H<sub>2</sub> generation, *International Journal of Hydrogen Energy*. 42 (2017) 8418–8449. <https://doi.org/10.1016/j.ijhydene.2016.12.052>.
- [2] M.N. Chong, B. Jin, C.W.K. Chow, C. Saint, Recent developments in photocatalytic water treatment technology: A review, *Water Research*. 44 (2010) 2997–3027. <https://doi.org/10.1016/j.watres.2010.02.039>.
- [3] Y.W. Phuan, W.-J. Ong, M.N. Chong, J.D. Ocon, Prospects of electrochemically synthesized hematite photoanodes for photoelectrochemical water splitting: A review, *Journal of Photochemistry and Photobiology C: Photochemistry Reviews*. 33 (2017) 54–82. <https://doi.org/10.1016/j.jphotochemrev.2017.10.001>.
- [4] J. Joy, J. Mathew, S.C. George, Nanomaterials for photoelectrochemical water splitting – review, *International Journal of Hydrogen Energy*. 43 (2018) 4804–4817. <https://doi.org/10.1016/j.ijhydene.2018.01.099>.
- [5] S. Sagadevan, Recent trends on nanostructures based solar energy applications : a review, *Rev. Adv. Matter. Science*. 43 (2013) 44–61.
- [6] X. Li, R. Shen, S. Ma, X. Chen, J. Xie, Graphene-based heterojunction photocatalysts, *Applied Surface Science*. 430 (2018) 53–107. <https://doi.org/10.1016/j.apsusc.2017.08.194>.
- [7] Y. Zhang, J. Lu, M.R. Hoffmann, Q. Wang, Y. Cong, Q. Wang, H. Jin, Synthesis of g-C<sub>3</sub>N<sub>4</sub>/Bi<sub>2</sub>O<sub>3</sub>/TiO<sub>2</sub> composite nanotubes: enhanced activity under visible light irradiation and improved photoelectrochemical activity, *RSC Adv*. 5 (2015) 48983–48991. <https://doi.org/10.1039/C5RA02750K>.
- [8] S. Hernández, D. Hidalgo, A. Sacco, A. Chiodoni, A. Lamberti, V. Cauda, E. Tresso, G. Saracco, Comparison of photocatalytic and transport properties of TiO<sub>2</sub> and ZnO nanostructures for solar-driven water splitting, *Phys. Chem. Chem. Phys*. 17 (2015) 7775–7786. <https://doi.org/10.1039/C4CP05857G>.
- [9] R. Zamiri, H.A. Ahangar, D.M. Tobaldi, A. Rebelo, M.P. Seabra, M. Shabani, J.M.F. Ferreira, Fabricating and characterising ZnO–ZnS–Ag<sub>2</sub>S ternary nanostructures with efficient solar-light photocatalytic

- activity, *Phys. Chem. Chem. Phys.* 16 (2014) 22418–22425. <https://doi.org/10.1039/C4CP02945C>.
- [10] A. Zaleska-Medynska, 1 - Introduction, in: A. Zaleska-Medynska (Ed.), *Metal Oxide-Based Photocatalysis*, Elsevier, 2018: pp. 1–2. <https://doi.org/10.1016/B978-0-12-811634-0.00001-9>.
- [11] A. Fujishima, K. Honda, Electrochemical Photolysis of Water at a Semiconductor Electrode, *Nature*. 238 (1972) 37–38. <https://doi.org/10.1038/238037a0>.
- [12] P.V. Kamat, Meeting the Clean Energy Demand: Nanostructure Architectures for Solar Energy Conversion, *J. Phys. Chem. C*. 111 (2007) 2834–2860. <https://doi.org/10.1021/jp066952u>.
- [13] M. Willander, O. Nur, Q.X. Zhao, L.L. Yang, M. Lorenz, B.Q. Cao, J.Z. Pérez, C. Czekalla, G. Zimmermann, M. Grundmann, A. Bakin, A. Behrends, M. Al-Suleiman, A. El-Shaer, A.C. Mofor, B. Postels, A. Waag, N. Boukos, A. Travlos, H.S. Kwack, J. Guinard, D.L.S. Dang, Zinc oxide nanorod based photonic devices: recent progress in growth, light emitting diodes and lasers, *Nanotechnology*. 20 (2009) 332001. <https://doi.org/10.1088/0957-4484/20/33/332001>.
- [14] H. Moussa, E. Girot, K. Mozet, H. Alem, G. Medjahdi, R. Schneider, ZnO rods/reduced graphene oxide composites prepared via a solvothermal reaction for efficient sunlight-driven photocatalysis, *Applied Catalysis B: Environmental*. 185 (2016) 11–21. <https://doi.org/10.1016/j.apcatb.2015.12.007>.
- [15] C.H.R. Paula, N.F. Andrade Neto, L.M.P. Garcia, R.M. Nascimento, C.A. Paskocimas, M.R.D. Bomio, F.V. Motta, Increased Degradation Capacity of Methylene Blue Dye Using Mg-doped ZnO Nanoparticles Decorated by Ag<sub>0</sub> Nanoparticles, *Journal of Elec Materi.* 48 (2019) 3017–3025. <https://doi.org/10.1007/s11664-019-07059-z>.
- [16] S.G. Kumar, K.S.R.K. Rao, Zinc oxide based photocatalysis: tailoring surface-bulk structure and related interfacial charge carrier dynamics for better environmental applications, *RSC Adv.* 5 (2014) 3306–3351. <https://doi.org/10.1039/C4RA13299H>.
- [17] S. Sittichai, A. Phuruangrat, T. Thongtem, S. Thongtem, Influence of Mg dopant on photocatalytic properties of Mg-doped ZnO nanoparticles prepared by sol–gel method, *Journal of the Ceramic Society of Japan*. 125 (2017) 122–124. <https://doi.org/10.2109/jcersj2.16202>.
- [18] N.H. Hashim, S. Subramani, M. Devarajan, A.R. Ibrahim, Properties of undoped ZnO and Mg doped ZnO thin films by sol-gel method

- for optoelectronic applications, *Journal of the Australian Ceramic Society*. 53 (2017) 421–431. <https://doi.org/10.1007/s41779-017-0051-9>.
- [19] C.-F. Liu, Y.-J. Lu, C.-C. Hu, Effects of Anions and pH on the Stability of ZnO Nanorods for Photoelectrochemical Water Splitting, *ACS Omega*. 3 (2018) 3429–3439. <https://doi.org/10.1021/acsomega.8b00214>.
- [20] R.E. Adam, G. Pozina, M. Willander, O. Nur, Synthesis of ZnO nanoparticles by co-precipitation method for solar driven photodegradation of Congo red dye at different pH, *Photonics and Nanostructures - Fundamentals and Applications*. 32 (2018) 11–18. <https://doi.org/10.1016/j.photonics.2018.08.005>.
- [21] C. Abed, C. Bouzidi, H. Elhouichet, B. Gelloz, M. Ferid, Mg doping induced high structural quality of sol–gel ZnO nanocrystals: Application in photocatalysis, *Applied Surface Science*. 349 (2015) 855–863. <https://doi.org/10.1016/j.apsusc.2015.05.078>.
- [22] M. Willander, O. Nur, J.R. Sadaf, M.I. Qadir, S. Zaman, A. Zainelabdin, N. Bano, I. Hussain, Luminescence from Zinc Oxide Nanostructures and Polymers and their Hybrid Devices, *Materials*. 3 (2010) 2643–2667. <https://doi.org/10.3390/ma3042643>.
- [23] C.H. Ahn, Y.Y. Kim, D.C. Kim, S.K. Mohanta, H.K. Cho, A comparative analysis of deep level emission in ZnO layers deposited by various methods, *Journal of Applied Physics*. 105 (2009) 013502. <https://doi.org/10.1063/1.3054175>.
- [24] S. Baruah, S.S. Sinha, B. Ghosh, S.K. Pal, A.K. Raychaudhuri, J. Dutta, Photoreactivity of ZnO nanoparticles in visible light: Effect of surface states on electron transfer reaction, *Journal of Applied Physics*. 105 (2009) 074308. <https://doi.org/10.1063/1.3100221>.
- [25] A.K. Chandiran, M. Abdi-Jalebi, M.K. Nazeeruddin, M. Grätzel, Analysis of Electron Transfer Properties of ZnO and TiO<sub>2</sub> Photoanodes for Dye-Sensitized Solar Cells, *ACS Nano*. 8 (2014) 2261–2268. <https://doi.org/10.1021/nn405535j>.
- [26] S. Hernández, V. Cauda, A. Chiodoni, S. Dallorto, A. Sacco, D. Hidalgo, E. Celasco, C.F. Pirri, Optimization of 1D ZnO@TiO<sub>2</sub> Core–Shell Nanostructures for Enhanced Photoelectrochemical Water Splitting under Solar Light Illumination, *ACS Appl. Mater. Interfaces*. 6 (2014) 12153–12167. <https://doi.org/10.1021/am501379m>.



- [27] C. Han, M.-Q. Yang, B. Weng, Y.-J. Xu, Improving the photocatalytic activity and anti-photocorrosion of semiconductor ZnO by coupling with versatile carbon, *Physical Chemistry Chemical Physics*. 16 (2014) 16891–16903. <https://doi.org/10.1039/C4CP02189D>.
- [28] UV light photocatalytic degradation of organic dyes with Fe-doped ZnO nanoparticles | Elsevier Enhanced Reader, (n.d.). <https://doi.org/10.1016/j.spmi.2014.06.013>.
- [29] X. Qiu, L. Li, J. Zheng, J. Liu, X. Sun, G. Li, Origin of the Enhanced Photocatalytic Activities of Semiconductors: A Case Study of ZnO Doped with Mg<sup>2+</sup>, (2008). <https://doi.org/10.1021/jp803129e>.
- [30] X. Qiu, G. Li, X. Sun, L. Li, X. Fu, Doping effects of Co<sup>2+</sup> ions on ZnO nanorods and their photocatalytic properties, *Nanotechnology*. 19 (2008) 215703. <https://doi.org/10.1088/0957-4484/19/21/215703>.
- [31] K. Pradeev raj, K. Sadaiyandi, A. Kennedy, S. Sagadevan, Z.Z. Chowdhury, Mohd.R.B. Johan, F.A. Aziz, R.F. Rafique, R. Thamiz Selvi, R. Rathina bala, Influence of Mg Doping on ZnO Nanoparticles for Enhanced Photocatalytic Evaluation and Antibacterial Analysis, *Nanoscale Res Lett*. 13 (2018) 229. <https://doi.org/10.1186/s11671-018-2643-x>.
- [32] J. Singh, P. Kumar, K.S. Hui, K.N. Hui, K. Ramam, R.S. Tiwari, O.N. Srivastava, Synthesis, band-gap tuning, structural and optical investigations of Mg doped ZnO nanowires, *CrystEngComm*. 14 (2012) 5898–5904. <https://doi.org/10.1039/C2CE06650E>.
- [33] C. Chen, W. Mei, W. Yu, X. Chen, L. Zeng, Y. Tsang, Z. Chao, X. Liu, Enhanced sunlight-driven photocatalytic property of Mg-doped ZnO nanocomposites with three-dimensional graphene oxide/MoS<sub>2</sub> nanosheet composites, *RSC Advances*. 8 (2018) 17399–17409. <https://doi.org/10.1039/C8RA02382D>.
- [34] J. Liqiang, W. Baiqi, X. Baifu, L. Shudan, S. Keying, C. Weimin, F. Honggang, Investigations on the surface modification of ZnO nanoparticle photocatalyst by depositing Pd, *Journal of Solid State Chemistry*. 177 (2004) 4221–4227. <https://doi.org/10.1016/j.jssc.2004.08.016>.
- [35] J. Xu, Y. Cui, Y. Han, M. Hao, X. Zhang, ZnO–graphene composites with high photocatalytic activities under visible light, *RSC Adv*. 6 (2016) 96778–96784. <https://doi.org/10.1039/C6RA19622E>.
- [36] R. Vinoth, P. Karthik, C. Muthamizhchelvan, B. Neppolian, M. Ashokkumar, Carrier separation and charge transport characteristics

- of reduced graphene oxide supported visible-light active photocatalysts, *Physical Chemistry Chemical Physics*. 18 (2016) 5179–5191. <https://doi.org/10.1039/C5CP08041J>.
- [37] H. Sun, S. Wang, Research Advances in the Synthesis of Nanocarbon-Based Photocatalysts and Their Applications for Photocatalytic Conversion of Carbon Dioxide to Hydrocarbon Fuels, *Energy & Fuels*. 28 (2014) 22–36. <https://doi.org/10.1021/ef401426x>.
- [38] S. Lee, D.A. Reddy, T. Kyu Kim, Well-wrapped reduced graphene oxide nanosheets on Nb<sub>3</sub>O<sub>7</sub>(OH) nanostructures as good electron collectors and transporters for efficient photocatalytic degradation of rhodamine B and phenol, *RSC Advances*. 6 (2016) 37180–37188. <https://doi.org/10.1039/C6RA05169C>.
- [39] J. Choi, D.A. Reddy, M.J. Islam, R. Ma, T.K. Kim, Self-assembly of CeO<sub>2</sub> nanostructures/reduced graphene oxide composite aerogels for efficient photocatalytic degradation of organic pollutants in water, *Journal of Alloys and Compounds*. 688 (2016) 527–536. <https://doi.org/10.1016/j.jallcom.2016.07.236>.
- [40] A. Kołodziejczak-Radzimska, T. Jesionowski, Zinc Oxide—From Synthesis to Application: A Review, *Materials*. 7 (2014) 2833–2881. <https://doi.org/10.3390/ma7042833>.
- [41] E.A.S. Dimapilis, C.-S. Hsu, R.M.O. Mendoza, M.-C. Lu, Zinc oxide nanoparticles for water disinfection, *Sustainable Environment Research*. 28 (2018) 47–56. <https://doi.org/10.1016/j.serj.2017.10.001>.
- [42] R.E. Adam, H. Alnoor, G. Pozina, X. Liu, M. Willander, O. Nur, Synthesis of Mg-doped ZnO NPs via a chemical low-temperature method and investigation of the efficient photocatalytic activity for the degradation of dyes under solar light, *Solid State Sciences*. 99 (2020) 106053. <https://doi.org/10.1016/j.solidstatesciences.2019.106053>.
- [43] A. Savoyant, M. Rollo, M. Texier, R.E. Adam, S. Bernardini, O. Pilon, O. Margeat, O. Nur, M. Willander, S. Bertaina, Light-induced high-spin state in ZnO nanoparticles, *Nanotechnology*. 31 (2019) 095707. <https://doi.org/10.1088/1361-6528/ab57f1>.
- [44] L. Larbi, H. Zouihri, Preparation of ZnO Nanoparticles without Any Annealing and Ripening Treatment, *Journal of Material Science and Engineering A*. (2011) 985–990.

- [45] G. Oskam, Metal oxide nanoparticles: synthesis, characterization and application, *J Sol-Gel Sci Technol.* 37 (2006) 161–164. <https://doi.org/10.1007/s10971-005-6621-2>.
- [46] R. Wahab, S.G. Ansari, Y.S. Kim, M. Song, H.-S. Shin, The role of pH variation on the growth of zinc oxide nanostructures, *Applied Surface Science.* 255 (2009) 4891–4896. <https://doi.org/10.1016/j.apsusc.2008.12.037>.
- [47] V. Etacheri, R. Roshan, V. Kumar, Mg-Doped ZnO Nanoparticles for Efficient Sunlight-Driven Photocatalysis, *ACS Appl. Mater. Interfaces.* 4 (2012) 2717–2725. <https://doi.org/10.1021/am300359h>.
- [48] N.H. Hashim, S. Subramani, M. Devarajan, A.R. Ibrahim, Properties of undoped ZnO and Mg doped ZnO thin films by sol-gel method for optoelectronic applications, *J Aust Ceram Soc.* 53 (2017) 421–431. <https://doi.org/10.1007/s41779-017-0051-9>.
- [49] Mohd. Arshad, Mohd. Meenhaz Ansari, A.S. Ahmed, P. Tripathi, S.S.Z. Ashraf, A.H. Naqvi, A. Azam, Band gap engineering and enhanced photoluminescence of Mg doped ZnO nanoparticles synthesized by wet chemical route, *Journal of Luminescence.* 161 (2015) 275–280. <https://doi.org/10.1016/j.jlumin.2014.12.016>.
- [50] S.V. Elangovan, N. Sivakumar, V. Chandramohan, Magnesium doped zinc oxide nanocrystals for photo-catalytic applications, *Journal of Materials Science: Materials in Electronics.* 26 (2015) 8753–8759. <https://doi.org/10.1007/s10854-015-3553-7>.
- [51] A. Kumar, K.L. Reddy, S. Kumar, A. Kumar, V. Sharma, V. Krishnan, Rational Design and Development of Lanthanide-Doped NaYF<sub>4</sub>@CdS–Au–RGO as Quaternary Plasmonic Photocatalysts for Harnessing Visible–Near-Infrared Broadband Spectrum, *ACS Appl. Mater. Interfaces.* 10 (2018) 15565–15581. <https://doi.org/10.1021/acsami.7b17822>.
- [52] R.E. Adam, E. Chalanger, M. Pirhashemi, G. Pozina, X. Liu, J. Palisaitis, H. Pettersson, M. Willander, O. Nur, Graphene-based plasmonic nanocomposites for highly enhanced solar-driven photocatalytic activities, *RSC Adv.* 9 (2019) 30585–30598. <https://doi.org/10.1039/C9RA06273D>.
- [53] E. Chalanger, H. Machhadani, S.-H. Lim, K.F. Karlsson, O. Nur, Magnus Willander, H. Pettersson, Influence of morphology on electrical and optical properties of graphene/Al-doped ZnO-nanorod composites, *Nanotechnology.* 29 (2018) 415201. <https://doi.org/10.1088/1361-6528/aad3ec>.

- [54] N. Zhang, Y. Zhang, Y.-J. Xu, Recent progress on graphene-based photocatalysts: current status and future perspectives, *Nanoscale*. 4 (2012) 5792–5813. <https://doi.org/10.1039/c2nr31480k>.
- [55] Q. Xiang, J. Yu, M. Jaroniec, Graphene -based semiconductor photocatalysts, *Chemical Society Reviews*. 41 (2012) 782–796. <https://doi.org/10.1039/C1CS15172J>.
- [56] B. Li, T. Liu, Y. Wang, Z. Wang, ZnO/graphene-oxide nanocomposite with remarkably enhanced visible-light-driven photocatalytic performance, *Journal of Colloid and Interface Science*. 377 (2012) 114–121. <https://doi.org/10.1016/j.jcis.2012.03.060>.
- [57] B. Li, H. Cao, ZnO@graphene composite with enhanced performance for the removal of dye from water, *Journal of Materials Chemistry*. 21 (2011) 3346–3349. <https://doi.org/10.1039/C0JM03253K>.
- [58] M.J. Allen, V.C. Tung, R.B. Kaner, Honeycomb Carbon: A Review of Graphene, *Chem. Rev.* 110 (2010) 132–145. <https://doi.org/10.1021/cr900070d>.
- [59] R. E. Adam, M. Pirhashemi, S. Elhag, X. Liu, A. Habibi-Yangjeh, M. Willander, O. Nur, ZnO/Ag/Ag<sub>2</sub>WO<sub>4</sub> photo-electrodes with plasmonic behavior for enhanced photoelectrochemical water oxidation, *RSC Advances*. 9 (2019) 8271–8279. <https://doi.org/10.1039/C8RA10141H>.
- [60] K.L. Reddy, S. Kumar, A. Kumar, V. Krishnan, Wide spectrum photocatalytic activity in lanthanide-doped upconversion nanophosphors coated with porous TiO<sub>2</sub> and Ag-Cu bimetallic nanoparticles, *Journal of Hazardous Materials*. 367 (2019) 694–705. <https://doi.org/10.1016/j.jhazmat.2019.01.004>.
- [61] M. Valenti, M. P. Jonsson, G. Biskos, A. Schmidt-Ott, W. A. Smith, Plasmonic nanoparticle-semiconductor composites for efficient solar water splitting, *Journal of Materials Chemistry A*. 4 (2016) 17891–17912. <https://doi.org/10.1039/C6TA06405A>.
- [62] Y. Tian, T. Tatsuma, Mechanisms and Applications of Plasmon-Induced Charge Separation at TiO<sub>2</sub> Films Loaded with Gold Nanoparticles, *J. Am. Chem. Soc.* 127 (2005) 7632–7637. <https://doi.org/10.1021/ja042192u>.
- [63] M. Pirhashemi, S. Elhag, R. E. Adam, A. Habibi-Yangjeh, X. Liu, M. Willander, O. Nur, n–n ZnO–Ag<sub>2</sub>CrO<sub>4</sub> heterojunction photoe-

- lectrodes with enhanced visible-light photoelectrochemical properties, *RSC Advances*. 9 (2019) 7992–8001. <https://doi.org/10.1039/C9RA00639G>.
- [64] X. Li, J. Yu, M. Jaroniec, Hierarchical photocatalysts, *Chemical Society Reviews*. 45 (2016) 2603–2636. <https://doi.org/10.1039/C5CS00838G>.
- [65] N. Sedaghati, A. Habibi-Yangjeh, M. Pirhashemi, S. Vadivel, Boosted visible-light photocatalytic performance of TiO<sub>2</sub>-x decorated by BiOI and AgBr nanoparticles, *Journal of Photochemistry and Photobiology A: Chemistry*. 384 (2019) 112066. <https://doi.org/10.1016/j.jphotochem.2019.112066>.
- [66] S. Feizpoor, A. Habibi-Yangjeh, I. Ahadzadeh, K. Yubuta, Oxygen-rich TiO<sub>2</sub> decorated with C-Dots: Highly efficient visible-light-responsive photocatalysts in degradations of different contaminants, *Advanced Powder Technology*. 30 (2019) 1183–1196. <https://doi.org/10.1016/j.appt.2019.03.014>.
- [67] R. E. Adam, M. Pirhashemi, S. Elhag, X. Liu, A. Habibi-Yangjeh, M. Willander, O. Nur, ZnO/Ag/Ag<sub>2</sub>WO<sub>4</sub> photo-electrodes with plasmonic behavior for enhanced photoelectrochemical water oxidation, *RSC Advances*. 9 (2019) 8271–8279. <https://doi.org/10.1039/C8RA10141H>.
- [68] S.-M. Lam, J.-C. Sin, A.Z. Abdullah, A.R. Mohamed, Degradation of wastewaters containing organic dyes photocatalysed by zinc oxide: a review, *Desalination and Water Treatment*. 41 (2012) 131–169. <https://doi.org/10.1080/19443994.2012.664698>.
- [69] J. Choi, D.A. Reddy, T.K. Kim, Enhanced photocatalytic activity and anti-photocorrosion of AgI nanostructures by coupling with graphene-analogue boron nitride nanosheets, *Ceramics International*. 41 (2015) 13793–13803. <https://doi.org/10.1016/j.ceramint.2015.08.062>.
- [70] D. Amaranatha Reddy, R. Ma, M.Y. Choi, T.K. Kim, Reduced graphene oxide wrapped ZnS–Ag<sub>2</sub>S ternary composites synthesized via hydrothermal method: Applications in photocatalyst degradation of organic pollutants, *Applied Surface Science*. 324 (2015) 725–735. <https://doi.org/10.1016/j.apsusc.2014.11.026>.
- [71] A. Sadollahkhani, I. Kazeminezhad, J. Lu, O. Nur, L. Hultman, M. Willander, Synthesis, structural characterization and photocatalytic application of ZnO@ZnS core–shell nanoparticles, *RSC Adv*. 4 (2014) 36940–36950. <https://doi.org/10.1039/C4RA05247A>.

- [72] R. Saleh, N.F. Djaja, UV light photocatalytic degradation of organic dyes with Fe-doped ZnO nanoparticles, Superlattices and Microstructures. 74 (2014) 217–233. <https://doi.org/10.1016/j.spmi.2014.06.013>.
- [73] Y. Li, X. Li, J. Li, J. Yin, Photocatalytic degradation of methyl orange by TiO<sub>2</sub>-coated activated carbon and kinetic study, Water Research. 40 (2006) 1119–1126. <https://doi.org/10.1016/j.watres.2005.12.042>.
- [74] W.A. Smith, Photoelectrochemical Cell Design, Efficiency, Definitions, Standards, and Protocols, in: S. Giménez, J. Bisquert (Eds.), Photoelectrochemical Solar Fuel Production: From Basic Principles to Advanced Devices, Springer International Publishing, Cham, 2016: pp. 163–197. [https://doi.org/10.1007/978-3-319-29641-8\\_4](https://doi.org/10.1007/978-3-319-29641-8_4).
- [75] T. Koida, S.F. Chichibu, A. Uedono, A. Tsukazaki, M. Kawasaki, T. Sota, Y. Segawa, H. Koinuma, Correlation between the photoluminescence lifetime and defect density in bulk and epitaxial ZnO, Appl. Phys. Lett. 82 (2003) 532–534. <https://doi.org/10.1063/1.1540220>.
- [76] R. Dom, H.G. Kim, P.H. Borse, Efficient hydrogen generation over (100)-oriented ZnO nanostructured photoanodes under solar light, CrystEngComm. 16 (2014) 2432–2439. <https://doi.org/10.1039/C3CE42058B>.
- [77] G. Will, ed., General Considerations, in: Powder Diffraction: The Rietveld Method and the Two Stage Method to Determine and Refine Crystal Structures from Powder Diffraction Data, Springer, Berlin, Heidelberg, 2006: pp. 1–39. [https://doi.org/10.1007/3-540-27986-5\\_1](https://doi.org/10.1007/3-540-27986-5_1).
- [78] A. Monshi, M.R. Foroughi, M.R. Monshi, Modified Scherrer Equation to Estimate More Accurately Nano-Crystallite Size Using XRD, WJNSE. 02 (2012) 154–160. <https://doi.org/10.4236/wjnse.2012.23020>.
- [79] J.F. Moulder, Handbook of X-ray Photoelectron Spectroscopy: A Reference Book of Standard Spectra for Identification and Interpretation of XPS Data, Physical Electronics, 1995.
- [80] M. Yoshikawa, K. Inoue, T. Nakagawa, H. Ishida, N. Hasuike, H. Harima, Characterization of ZnO nanoparticles by resonant Raman scattering and cathodoluminescence spectroscopies, Applied Physics Letters. 92 (2008) 113115. <https://doi.org/10.1063/1.2901159>.

- [81] M.R. Phillips, O. Gelhausen, E.M. Goldys, Cathodoluminescence properties of zinc oxide nanoparticles, *Physica Status Solidi (a)*. 201 (2004) 229–234. <https://doi.org/10.1002/pssa.200303977>.
- [82] S. Choi, M.R. Phillips, I. Aharonovich, S. Pornsuwan, B.C.C. Cowie, C. Ton-That, Photophysics of Point Defects in ZnO Nanoparticles, *Advanced Optical Materials*. 3 (2015) 821–827. <https://doi.org/10.1002/adom.201400592>.
- [83] V. Khranovskyy, V. Lazorenko, G. Lashkarev, R. Yakimova, Luminescence anisotropy of ZnO microrods, *Journal of Luminescence*. 132 (2012) 2643–2647. <https://doi.org/10.1016/j.jlumin.2012.04.048>.
- [84] C. Lu, Y. Wu, F. Mai, W. Chung, C. Wu, W. Lin, C. Chen, Degradation efficiencies and mechanisms of the ZnO-mediated photocatalytic degradation of Basic Blue 11 under visible light irradiation, *Journal of Molecular Catalysis A: Chemical*. 310 (2009) 159–165. <https://doi.org/10.1016/j.molcata.2009.06.011>.
- [85] A. Sadollahkhani, I. Kazeminezhad, J. Lu, O. Nur, L. Hultman, M. Willander, Synthesis, structural characterization and photocatalytic application of ZnO@ZnS core–shell nanoparticles, *RSC Advances*. 4 (2014) 36940–36950. <https://doi.org/10.1039/C4RA05247A>.
- [86] B. Panigrahy, M. Aslam, D. Bahadur, Aqueous Synthesis of Mn- and Co-Doped ZnO Nanorods, *J. Phys. Chem. C*. 114 (2010) 11758–11763. <https://doi.org/10.1021/jp102163b>.
- [87] V. Etacheri, R. Roshan, V. Kumar, Mg-Doped ZnO Nanoparticles for Efficient Sunlight-Driven Photocatalysis, *ACS Applied Materials & Interfaces*. 4 (2012) 2717–2725. <https://doi.org/10.1021/am300359h>.
- [88] S. Sitthichai, A. Phuruangrat, T. Thongtem, S. Thongtem, Influence of Mg dopant on photocatalytic properties of Mg-doped ZnO nanoparticles prepared by sol–gel method, *J. Ceram. Soc. Japan*. 125 (2017) 122–124. <https://doi.org/10.2109/jcersj2.16202>.
- [89] S.S. Hullavarad, N.V. Hullavarad, D.E. Pugel, S. Dhar, T. Venkatesan, R.D. Vispute, Structural and chemical analysis of pulsed laser deposited  $\text{Mg}_x\text{Zn}_{1-x}\text{O}$  hexagonal ( $x=0.15, 0.28$ ) and cubic ( $x=0.85$ ) thin films, *Optical Materials*. 30 (2008) 993–1000. <https://doi.org/10.1016/j.optmat.2007.05.027>.
- [90] S. Anandan, A. Vinu, K.L.P. Sheeja Lovely, N. Gokulakrishnan, P. Srinivasu, T. Mori, V. Murugesan, V. Sivamurugan, K. Ariga, Pho-

- tocatalytic activity of La-doped ZnO for the degradation of monocrotophos in aqueous suspension, *Journal of Molecular Catalysis A: Chemical*. 266 (2007) 149–157. <https://doi.org/10.1016/j.molcata.2006.11.008>.
- [91] D.M. Fragua, R. Abargues, P.J. Rodriguez-Canto, J.F. Sanchez-Royo, S. Agouram, J.P. Martinez-Pastor, Au–ZnO Nanocomposite Films for Plasmonic Photocatalysis, *Advanced Materials Interfaces*. 2 (n.d.) 1500156. <https://doi.org/10.1002/admi.201500156>.
- [92] D. Liu, W. Huang, L. Li, L. Liu, X. Sun, B. Liu, B. Yang, C. Guo, Experimental and theoretical investigation on photocatalytic activities of 1D Ag/Ag<sub>2</sub>WO<sub>4</sub> nanostructures, *Nanotechnology*. 28 (2017) 385702. <https://doi.org/10.1088/1361-6528/aa7d96>.
- [93] X. Yang, H. Li, W. Zhang, M. Sun, L. Li, N. Xu, J. Wu, J. Sun, High Visible Photoelectrochemical Activity of Ag Nanoparticle-Sandwiched CdS/Ag/ZnO Nanorods, *ACS Appl. Mater. Interfaces*. 9 (2017) 658–667. <https://doi.org/10.1021/acsami.6b12259>.
- [94] S. Zhang, Z. Liu, Y. Zhang, S. Gao, R. Jin, Q. Wang, Highly effective photoelectrochemical performance of solar energy materials based on Ag<sub>2</sub>WO<sub>4</sub>-AgX (X=Cl, Br, I) sensitized TiO<sub>2</sub> nanotube arrays, *Ceramics International*. 44 (2018) 6659–6665. <https://doi.org/10.1016/j.ceramint.2018.01.077>.





# Papers

The papers associated with this thesis have been removed for copyright reasons. For more details about these see:

<http://urn.kb.se/resolve?urn=urn:nbn:se:liu:diva-164334>

## **FACULTY OF SCIENCE AND ENGINEERING**

Linköping Studies in Science and Technology, Dissertation No. 2059, 2020  
Department of Science and Technology

Linköping University  
SE-581 83 Linköping, Sweden

[www.liu.se](http://www.liu.se)